International Journal of Plasticity 27 (2011) 1328–1354

Contents lists available at ScienceDirect

International Journal of Plasticity

journal homepage: www.elsevier.com/locate/ijplas

# Simulation of polycrystal deformation with grain and grain boundary effects

H. Lim [a], M.G. Lee [b], J.H. Kim [c], B.L. Adams [d], R.H. Wagoner [a,*]

[a] Department of Materials Science and Engineering, The Ohio State University, 2041 College Road, Columbus, OH 43210, USA
[b] Graduate Institute of Ferrous Technology, Pohang University of Science and Technology (POSTECH), San 31, Hyoja-dong, Nam-gu, Pohang, Gyeongbuk 790-784, Republic of Korea
[c] Materials Deformation Group, Korea Institute of Materials Science, 531 Changwondaero, Changwon, Gyeongnam 641-831, Republic of Korea
[d] Department of Mechanical Engineering, Brigham Young University Provo, UT 84601, USA

ARTICLE INFO

*Article history:*
Received 5 November 2010
Received in final revised form 25 February 2011
Available online 13 March 2011

*Keywords:*
Grain boundary
Hall–Petch law
Dislocation density
Meso-scale simulation

ABSTRACT

Modeling the strengthening effect of grain boundaries (Hall–Petch effect) in metallic polycrystals in a physically consistent way, and without invoking arbitrary length scales, is a long-standing, unsolved problem. A two-scale method to treat predictively the interactions of large numbers of dislocations with grain boundaries has been developed, implemented, and tested. At the first scale, a standard grain-scale simulation (GSS) based on a finite element (FE) formulation makes use of recently proposed dislocation-density-based single-crystal constitutive equations ("SCCE-D") to determine local stresses, strains, and slip magnitudes. At the second scale, a novel meso-scale simulation (MSS) redistributes the mobile part of the dislocation density within grains consistent with the plastic strain, computes the associated inter-dislocation back stress, and enforces local slip transmission criteria at grain boundaries.

Compared with a standard crystal plasticity finite element (FE) model (CP-FEM), the two-scale model required only 5% more CPU time, making it suitable for practical material design. The model confers new capabilities as follows:

(1) The two-scale method reproduced the dislocation densities predicted by analytical solutions of single pile-ups.
(2) Two-scale simulations of 2D and 3D arrays of regular grains predicted Hall–Petch slopes for iron of $1.2 \pm 0.3$ MN/m$^{3/2}$ and $1.5 \pm 0.3$ MN/m$^{3/2}$, in agreement with a measured slope of $0.9 \pm 0.1$ MN/m$^{3/2}$.
(3) The tensile stress–strain response of coarse-grained Fe multi-crystals (9–39 grains) was predicted 2–4 times more accurately by the two-scale model as compared with CP-FEM or Taylor-type texture models.
(4) The lattice curvature of a deformed Fe-3% Si columnar multi-crystal was predicted and measured. The measured maximum lattice curvature near grain boundaries agreed with model predictions within the experimental scatter.



* Corresponding author. Tel.: +1 614 292 2079; fax: +1 614 292 6530.
*E-mail address:* wagoner.2@osu.edu (R.H. Wagoner).

0749-6419/$ - see front matter © 2011 Elsevier Ltd. All rights reserved.
doi:10.1016/j.ijplas.2011.03.001

## 1. Introduction

Nearly all structural metals and alloys are polycrystalline. That is, they are assemblies of crystals (or grains), usually with sizes from 1 μm to many μm, that have properties different than those of the grains themselves. This can readily be seen in terms of the Hall–Petch effect, which is embodied in the following equation (Hall, 1951; Petch, 1953):

$$\sigma_y = \sigma_0 + k_y D^{-1/2}, \tag{1}$$

where $\sigma_y$ and $D$ are the yield stress and the mean grain size of the material, respectively, and $\sigma_0$ and $k_y$ are material constants usually referred to as the friction stress and the Hall–Petch slope, respectively. Hall–Petch slopes measured for specified ranges of grain sizes are shown in Table 1 for various FCC, BCC and HCP polycrystals. For FCC materials, $k_y$ values are generally less than 0.3 MN/m$^{3/2}$ while those for BCC materials are higher by a factor of 2–3. Over a readily-attainable range of grain sizes (2–40 μm), 0.13 wt.% carbon steels shows a change of strength by a factor of 2.5 (Meyers and Chawla, 1998).

In spite of the obvious importance of the grain and grain boundary structure on the mechanical performance of metals, prediction of the effect with a physically realistic model has not been attained. For this reason, material design, while advanced in many aspects, does not currently include grain boundary effects in a predictive way. Phenomenological models and simulation techniques applicable to the polycrystal problem, along with their limitations, are reviewed briefly here. The body of this paper introduces a new method that predicts Hall–Petch slopes and is consistent with known structure and behavior of non-nano polycrystals.

### 1.1. Phenomenological models of the Hall–Petch effect

The earliest, simplest, and nearly the only predictive description of the Hall–Petch effect was proposed by Hall and Petch based on the idea of a dislocation pile-up (Hall, 1951; Petch, 1953). The role of grain boundaries as obstacles to dislocation motion is invoked; dislocations pass through grain boundaries or nucleate dislocations in the neighboring grain when the stress at the head of the pile-up exceeds a critical obstacle stress, $\tau_{obs}$. The pile-up length, $l$, is linearly related to the number of dislocations in the pile-up, as is readily derived (Leibfried, 1951; Esheby et al., 1951; Hirth and Lothe, 1969)

$$l = \frac{\mu b n}{\pi k \tau_a}, \tag{2}$$

**Table 1**
Hall–Petch slopes, $k_y$, based on initial yield stresses for metal polycrystals with three crystal structures.

| | Material | $k_y$ (MN/m$^{3/2}$) | $D$ (μm) | References |
|---|---|---|---|---|
| BCC | Fe-3% Si | 0.82–1.08 | 19–1250 | Hull (1975), Abson and Jonas (1970) |
| | Iron | 0.88 | 60–1350 | (Current work) |
| | Mild Steel | 0.51–0.74 | 2–250 | Armstrong et al. (1962); Abson and Jonas (1970) |
| | UFGF/CH Steel | 0.07 | 0.7–6 | Zhao et al. (2006) |
| | IF Steel | 0.14 | 0.2–10 | Tsuji et al. (2001) |
| | Spheroidized steel | 0.41–0.58 | 5–12 | Anand and Gurland (1976) |
| | Carbon steels (0.03% C) | 0.81 | 15–91 | Chang and Preban (1985) |
| | Carbon steels (0.07% C) | 0.88 | 3–38 | Chang and Preban (1985) |
| | Carbon steels (0.17% C) | 1.21 | 6–60 | Chang and Preban (1985) |
| | Carbon steels (0.23% C) | 1.58 | 6–65 | Chang and Preban (1985) |
| | Tantalum | 0.23–0.60 | 2–250 | Koo (1962); Zerilli and Armstrong (1990) |
| | Chromium | 0.90 | 32–1000 | Marcinkowski and Lipsitt (1962) |
| | Molybdenum | 1.77 | 28–250 | Johnson (1959) |
| | Tungsten | 0.79 | 0.3–5 | Meieran and Thomas (1965) |
| | Vanadium | 0.30 | 2–27 | Lindley and Smallman (1963) |
| | Niobium | 0.04 | 48–1414 | Adams et al. (1960) |
| Avg. | 0.73 | | | |
| FCC | 310 Austenitic steel | 0.24 | 1–63 | Grabski and Wyrzylowski (1980) |
| | Silver | 0.07 | 14–250 | Carreker (1957) |
| | Aluminum | 0.07–0.11 | 2–200 | Carreker and Hibbard (1957) and Abson and Jonas (1970) |
| | Al – 4.5% Cu | 0.19–0.47 | 15–170 | Zoqui and Robert (1998) |
| | Al – 3.5% Mg | 0.26 | 18–180 | Philips and Swain (1952) |
| | Copper | 0.11 | 3–32 | Feltham and Meakin (1957) |
| | Cu – 3.2% Sn | 0.19 | 3–110 | Russell (1965) |
| | Cu – 30% Sn | 0.31 | – | Armstrong et al. (1962) |
| | Ni – 1.2% Al | 0.19–0.88 | 13–387 | Nembach (1990) |
| Avg. | 0.26 | | | |
| HCP | Zinc ($\varepsilon_p$ = 0.005, 0 °C) | 0.22 | 28–110 | Armstrong et al. (1962) |
| | Magnesium | 0.28 | 26–1000 | Hauser et al. (1956) |
| | Zirconium | 0.25 | 3–84 | Keeler (1955) |
| | Beryllium | 0.41 | 80–340 | Allen and Moore (1963) |
| | Titanium | 0.40 | – | Meyers and Chawla (1998) |
| Avg. | 0.31 | | | |

where $\tau_a$ is the applied shear stress, $\mu$ is the shear modulus and $b$ is the Burgers vector of each dislocation in the pile-up. $k$ represents the character of the dislocations, with $k = 1$ for screw dislocations and $k = 1 - \nu$ ($\sim$0.7) for edge dislocations. The tip stress at the head of the pile-up is given by $\tau_{tip} = n\tau_a$ and accounting for the friction stress, $\sigma_0$, leads to the following form of Eq. (1) (Hirth and Lothe, 1969):

$$\sigma = \sigma_0 + M\left(\frac{\mu b \tau_{obs}}{\pi k}\right)^{1/2} D^{-1/2}, \tag{3}$$

where $M$ is the Taylor factor ($\sim$3), and $D$, the grain size, is assumed to determine the pile-up length, i.e. $D = l$ or $D = \frac{1}{\alpha} l$ where $\alpha$ is a constant greater than or equal to 1. $\tau_{obs}$ is the critical value of the stress acting on the lead dislocation that must be exceeded in order to propel the lead dislocation through the obstacle.

Eq. (3) represents an appealingly simple, predictive equation that in principle can be tested against experiment. The power of $D$, $-1/2$, is verified approximately by many experiments, although the precision of the result leads to a range of $-0.3$ to $-1$ for "normal" (i.e. non-nano) grain sizes (Kocks, 1959).

There are several conceptual problems with the physical basis underlying Eq. (3): (1) pile-ups are seldom seen in most polycrystals, (2) when pile-ups are seen (i.e. at very low strain, for low stacking fault FCC materials), they do not extend across a grain or sizable fraction of a grain but instead are local to a grain boundary (Feaugas and Haddou, 1999, 2003; Saada, 2005), (3) the Hall–Petch slope for the ultimate tensile strength (i.e. at higher strain) is usually higher than for the yield stress, although pile-ups are not seen at larger strain, (4) materials with the highest Hall–Petch slopes, e.g. BCC Fe, have high stacking fault energies that permits easy cross-slip rather than the formation of co-planar pile-ups (and linear slip traces) (Li and Chou, 1970; Hull, 1975). Therefore, while the pile-up model captures the essence of the role of grain boundaries as obstacles to dislocation motion, the detailed microstructural basis leading to Eq. (3) is not satisfied. Furthermore, the simple pile-up model makes no connection to dislocation densities and its spatial redistribution consistent with strain.

The main uncertainty in this quantitative prediction of Eq. (3) is the value of $\tau_{obs}$, which has seldom been measured. In one set of published measurements (Shen et al., 1986), for 304 stainless steel (FCC), a value of $\tau_{obs}$ equal to 5 times the yield stress of the polycrystal was obtained. (See Section 2.2 for calculation of this number.) Using this ratio for other materials, along with an average Taylor factor of $M = 3$, a comparison of Eq. (3) and experimental values of the Hall–Petch slope were obtained as shown in Table 2. While for isolated cases, i.e. FCC Cu, the prediction is reasonable, for materials with higher Hall–Petch slopes, Eq. (3) underpredicts the effect by a factor of 2–5. For BCC Fe, the prediction is one fifth of the measurement. While the form of Eq. (3) is confirmed experimentally, the quantitative prediction is not verified for typical materials.

More recent models of the Hall–Petch effect rely on undetermined constants (usually length scales) that are not amenable to quantitative verification. In the "composite model", each grain is described as a composite material with the soft bulk region and the hard grain boundary layer (Kocks, 1970; Hirth, 1972; Meyers and Ashworth, 1982). The overall flow stress is obtained using a simple law of mixture for the two materials. The "smaller is stronger" grain size effect is a result of assuming an arbitrary, constant grain boundary width (i.e. a new length scale) that can be chosen to reproduce Hall–Petch plots. The grain boundary widths and their constancy have not generally been measured independently. Therefore, such models cannot be considered predicting, certainly not quantitatively.

Strain-gradient models reproduce the Hall–Petch effect using the well-known result that flow stress is proportional to the square root of dislocation density (Taylor, 1934) by hypothesizing that smaller grains require more geometrically necessary dislocations. This concept can be introduced directly by an arbitrary addition of GND content inverse to grain size (Cottrell, 1953; Conrad, 1961, 1970; Li, 1963; Ashby, 1970) or via continuum constitutive equations coupled to an arbitrary length scale representing the microstructure size (Fleck et al., 1994; Fleck and Hutchinson, 1997; Nix and Gao, 1998; Gurtin, 2000, 2002; Gao et al., 1999; Huang et al., 2000; Abu Al-Rub and Voyiadijus, 2006). The latter models introduce size dependence by a material length-scale parameter related to strain gradient, estimated from experiments such as indentation (Nix and Gao, 1998), torsion (Fleck et al., 1994) or bend tests (Stolken and Evans, 1998). However, the physical origin of this length scale parameter is not clear. Other versions compute the gradient effect directly but introduce an arbitrary length scale representing the width of the grain boundary (Evers et al., 2002) or avoid the arbitrary length scale by invoking a procedure so computationally intensive that only an idealized single crystal with single slip can be simulated (Arsenlis et al., 2004). Therefore, current strain-gradient approaches do not produce predictions suitable for experimental verification because either (a) they invoke an arbitrary length scale whose physical origin is murky or unmeasurable, and/or (b) they rely on no known, measurable properties of grain boundaries as sources or obstacles to dislocation motion.

**Table 2**
Measured Hall–Petch slopes compared with ones computed using the original pileup model and an obstacle stress five times the yield stress (unit: MN/m$^{3/2}$).

| | Material | Calculated $k_c$ | Measured $k$ | $k/k_c$ |
|---|---|---|---|---|
| FCC | Aluminum | 0.05 | 0.07–0.11 Carreker and Hibbard (1957) and Abson and Jonas (1970) | 1.4–2.2 |
| | Copper | 0.09 | 0.11 Feltham and Meakin (1957) | 1.2 |
| HCP | Magnesium | 0.05 | 0.28 Hauser et al. (1956) | 5.6 |
| | Titanium | 0.16 | 0.40 Meyers and Chawla (1998) | 2.5 |
| BCC | Iron | 0.18 | 0.88 (Current work) | 4.9 |

### 1.2. Related simulation approaches

Intensive simulations have been directed at a single dislocation approaching a well-characterized planar boundary. Such methods promise the ability to determine $\tau_{obs}$ without resort to a large-scale model fit to macroscopic yield stress measurements. Atomistic simulation obtained $\tau_{obs}$ for specific interfaces or grain boundaries for FCC metals (Hoagland et al., 2002, 2004; Hoagland and Kurtz, 2002; de Koning et al., 2003) but the accuracy relies on the fidelity of empirically obtained interatomic potentials (Hoagland et al., 2002). Dislocation dynamic simulations of the collective behavior of dislocations predict grain size dependence (Biner and Morris, 2003; Lefebvre et al., 2005, 2007; Ohashi et al., 2007; Balint et al., 2005, 2008) but utilize non-physical impenetrable grain boundary conditions or simplified slip systems. More recent 2D dislocation dynamic simulations (Li et al., 2009) take account of a penetrable grain boundary with $\tau_{obs}$ obtained from the grain boundary energy and strain energy of grain boundary debris, but only at strain rates ($2000\ s^{-1}$) inconsistent with Hall–Petch measurements, and time steps (0.5 ns) suitable only for submicron grain sizes.

Many simulations of polycrystals are based on texture analysis, where each grain is treated independent of the others except as linked by a simple law enforcing equal strain (Taylor, 1934), equal stress (Sachs, 1928; Parks and Ahzi, 1990), or combinations thereof (relaxed const., self consistent) (Canova et al., 1985; Kröner, 1961; Molinari et al.,1987). The only microstructural information used is the statistical distribution of grain orientation. While such methods predict plastic anisotropy and its evolution, particularly for FCC materials, they do not reproduce the Hall–Petch effect. Indeed, they are not informed by grain size, grain-to-grain relationships, grain boundary orientation, or slip system incompatibility across boundaries.

An improvement on texture methods is sometimes called CP-FEM (crystal plasticity finite element modeling). CP-FEM treats a small number of grains in a finite element sense, normally with many elements per grain and an orientation-dependent continuum constitutive equation (Becker and Panchanadeeswaran, 1995; Dawson et al., 2002; Sarma et al., 2002: Raabe et al., 2002; Delannay et al., 2009; Choi et al., 2010). Such methods allow enforcement of compatibility and equilibrium but do not predict an effect of grain size or grain boundary properties (except through minor elastic incompatibility effects) unless arbitrary length scales are introduced in the constitutive model, similar to strain gradient phenomenological models (Ma et al., 2006).

The current work proposes an efficient predictive model to simulate the deformation of metal polycrystals ($\sim$100 grains) of typical sizes (1–1000 μm), at normal strain rates. The two-scale model includes the effects of local grain boundary properties and the grain sizes (via $\tau_{obs}$), without relying on non-physical models (pile-ups) and without introducing arbitrary, undetermined length scales. Such a model, if proven successful, can open the door to a new level of material design taking into account grain shapes and sizes and grain boundary orientations and properties.

## 2. Simulation procedures

A two-stage simulation procedure was developed to simulate the interactions of large numbers of dislocations with grain boundaries for materials with grain sizes larger than a micron, thus avoiding nano-scale effects and the need to address individual, discrete dislocations. The intent is to be broadly predictive rather than merely descriptive; therefore the number of undetermined, arbitrary parameters was minimized for the initial treatment presented here.

The core of the proposed method relies on a standard finite element discretization of a polycrystal with numerous elements per grain, as shown in Fig. 1. Starting from an initial configuration (unloaded, undeformed state with initial homogeneous dislocation density equally distributed on all slip systems), external displacement increment boundary conditions are applied through ABAQUS/Standard (implicit) (Hibbit, 2005) techniques using a special material model with two sub-steps performed at each time step, as implemented through the UMAT subroutine capability. While the overall solution procedure is implicit, the two sub-steps, here called GSS and MSS, interact with each other explicitly. That is, the GSS and MSS are sequentially coupled, from time step to time step, in the first implementation. An iterative capability could be readily added.

The grain-scale simulation (GSS) follows well-established developments appearing in the literature (Peirce et al., 1983; Asaro and Needleman, 1985; Beaudoin et al., 1994; Sarma and Dawson, 1996; Dawson et al., 2002; Lee et al., 2010). Mechanical equilibrium is enforced while maintaining material compatibility in a finite element sense (i.e. at the nodes). The GSS computes inhomogeneous stress, strain, and slip activity, and, as inferred from slip magnitudes using established principles, the local generation of dislocation density on each slip system in each element. The three constants relating dislocation density to strain, i.e. strain hardening, are the only undetermined constants in the formulation. They are readily found from fitting a measured tensile stress–strain curve, ideally for a single crystal.

The novel meso-scale simulation (MSS) redistributes the mobile dislocation content for each slip system, as represented by a superdislocation at the center of each finite element. The mobile part of the dislocation density is defined by the minimum dislocation content that must be redistributed in order to accommodate the plastic strain and strain gradients determined from the GSS. The redistribution of mobile dislocation content modifies the flow stress and back stress in each element according to Orowan's equation and the elastic inter-dislocation interactions, respectively, which in turn alter the GSS results at the next time step. To be clear, the local total dislocation content (i.e. statistical and polar contributions) affects the slip resistance for each slip system in each element, while the polar, or mobile, content affects only the back stress. Fig. 2 shows the flow chart of the two-scale modeling scheme.

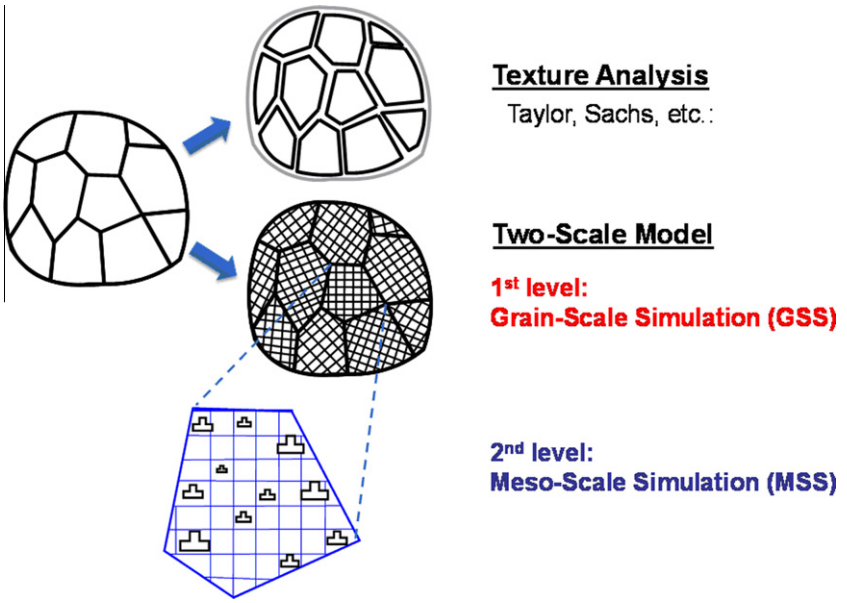


**Fig. 1.** Schematic view of typical texture analysis compared with the two-scale simulation procedure consisting of a grain-scale simulation (GSS) and meso-scale simulation (MSS).

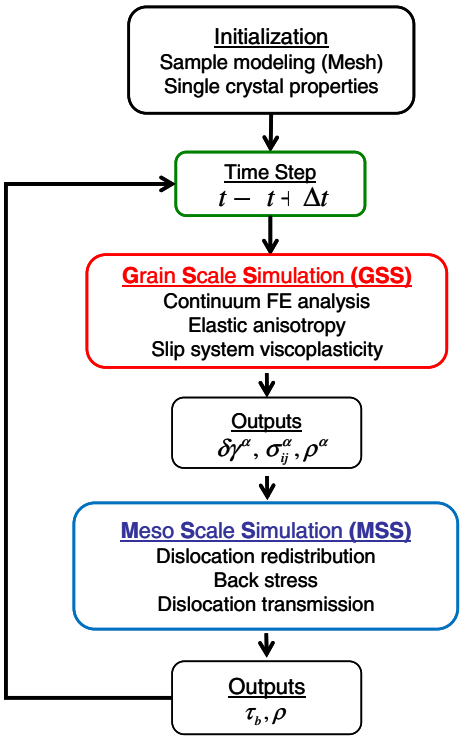


**Fig. 2.** A simplified flow chart illustrating the two-scale modeling scheme. An explicit procedure between the two scales is shown.

There are many choices among assumptions and parameters that must be made for a practical first implementation. The basic assumptions listed below were selected to eliminate all unknown parameters, except the three related to strain hardening as noted above.

Assumptions:

(1) All plastic deformation occurs only by slip on fixed slip systems; climb, twinning, grain boundary sliding, cross-slip and other mechanisms are ignored.

(2) Elastic image effects between the dislocation content and the boundaries are ignored, except as lumped into a grain boundary obstacle stress. The obstacle stress is the sole effect arising from plastic incompatibility.
(3) The dislocation density on a single slip system in a finite element can be lumped into a single superdislocation.
(4) The entire dislocation density has edge character such that the line direction is uniquely determined by slip plane and Burgers vector.
(5) For purposes of computing a back stress, dislocations interact only with other dislocations within the same slip system in a single grain. These interactions are approximated using isotropic elasticity.

These assumptions are consistent with the goal of providing a practical and effective scheme to account for the interactions of large numbers of dislocations with grain boundaries, and thus to *predict* phenomena such as the Hall–Petch effect (rather than fitting it). Note that all of these assumptions apply only to the new, novel MSS procedure. The GSS procedure is standard, and is based on well-established procedures.

Assumption 1 is normally accurate at low homologous temperatures for non-twinning alloys. Assumptions 2 and 3 are simplifications lumping the dislocation content within an element, or all grain boundary impediments into a single critical stress value, respectively, without considering the detailed local mechanisms. These are consistent with the meso-scale approach and finite element approximations. Assumptions 4 and 5 may require more consideration, as appears below. They are clearly not accurate in terms of the motion of individual dislocations, but the errors may not be significant in terms of the goal of the work and the focus on the meso-scale. The only reliable way to test the validity of these assumptions is by comparing simulations and measurements of polycrystal behavior. Such tests form a significant part of this paper.

Assumption 4 is clearly not correct, i.e. all dislocations are not edge dislocations. Furthermore, the dislocation character has been shown for some crystals and temperatures to affect mobility. However, it is not clear that this distinction is important for large populations of moving dislocations. For example, what differences would be expected if one could, hypothetically, enforce a dislocation population of all edge dislocations, or all screw dislocation, or half edge and half screw, or all mixed dislocations? With the possible exception of variations of yield and flow stresses, the differences are not clear. Typical single-crystal constitutive equations (Peirce et al., 1983) have found great utility and success, yet they ignore the character of the dislocations. The model introduced in this paper does not attempt to understand the fundamental underpinnings of single-crystal yield and strain hardening, only the elusive connection between those properties and the corresponding ones of polycrystals. The yield stress and form of strain hardening of single crystals represent all 3 of the fit parameters in the model. It should also be noted that Assumption 4 applies only to the MSS part of the two-scale procedure. In the GSS, the phenomenological law of dislocation generation and dislocation that is used is based on the total, general dislocation content.

Assumption 5 applies only to the MSS part of the simulation procedure. In the GSS, dislocations from all other slip system contribute to the strength and hardening of an active slip system. In the MSS procedure, only the long-range interactions of lumped dislocations at distances of thousands of Burgers vectors are considered. While like dislocations interact at large distances in a net non-zero way leading to a significant back stress (i.e. like a pile-up), it is unclear whether there is any significant back stress developed at large distances among a 3-D distribution of oblique dislocation lines, Burgers vectors, and slip planes. On average, it seems probable that such contributions are nearly symmetric (say, from above and below the slip plane being considered, or ahead and behind), making them vanishingly small, or second order, as compared with the interactions among dislocations on a single slip plane with the same Burgers vector and line directions.

### 2.1. Grain-scale simulation (GSS)

The GSS procedure follows well-established continuum mechanical principles in the literature (Lee, 1969; Rice, 1971; Hill and Rice, 1972; Asaro, 1979; Peirce et al., 1982). It is based on the classical crystal plasticity framework that the total deformation gradient at a material point within a crystal is described by a multiplicative decomposition (Lee, 1969)

$$\mathbf{F} = \mathbf{F}^e\mathbf{F}^p. \tag{4}$$

The velocity gradient, $\bar{\mathbf{L}}^p$, is represented in the intermediate configuration in terms of the sum of shear strain rates, $\dot{\gamma}^{(\alpha)}$, summed over the number of slip system, *NS* (Rice, 1971; Asaro, 1983)

$$\bar{\mathbf{L}}^p = \dot{\mathbf{F}}^p\mathbf{F}^{p-1} = \sum_{\alpha=1}^{NS} \dot{\gamma}^{(\alpha)}\mathbf{s}_0^{(\alpha)} \otimes \mathbf{n}_0^{(\alpha)}, \tag{5}$$

where $\mathbf{s}_0^{(\alpha)}$ and $\mathbf{n}_0^{(\alpha)}$ are the initial unit vectors of the slip direction and the slip plane normal direction on $\alpha$th slip system, respectively. For a strain-rate-dependent crystal model, the crystalline visco-plastic shear rate of the power-law form defined on the $\alpha$th slip system may be written as (Hutchinson, 1976; Peirce et al., 1982):

$$\dot{\gamma} = \dot{\gamma}_0\left(\left|\frac{\tau^{(\alpha)}}{g^{(\alpha)}}\right|\right)^{1/m} sign(\tau^{(\alpha)}), \tag{6}$$

where $\dot{\gamma}_0$ is a reference shear rate, $\tau^{(\alpha)}$ and $g^{(\alpha)}$ are the resolved shear stress and the slip resistance of $\alpha$th slip system, respectively and $m$ is the rate sensitivity exponent. $\dot{\gamma}_0 = 0.001\ s^{-1}$ and $m = 0.012$ were adopted from the literature, respectively (Bronkhorst et al., 1992; Kalidindi et al., 1992).

To this point, the constitutive equations mirror those used routinely for texture analysis and appearing in the literature. Those standard forms are referred to as the PAN constitutive model (Peirce, Asaro, Needleman) (Peirce et al., 1982). The evolution of $g^{(\alpha)}$ was formulated using novel single crystal constitutive equations based on dislocation density herein referred to briefly as SCCE-D (Lee et al., 2010). These constitutive equations were shown to represent single-crystal behavior accurately for both FCC and BCC metals (Lee et al., 2010). The remainder of this section outlines the development of the SCCE-D briefly, with reference to the original publication for detailed implementation and testing against measured single crystal behavior and PAN model predictions (Lee et al., 2010).

The dislocation density for SCCE-D in each slip system $\alpha$, $\rho^{(\alpha)}$, is computed explicitly for each element. Twenty-four slip systems for BCC material were considered: 12 of type $\langle 1\,1\,1\rangle\{1\,1\,0\}$ and 12 of type $\langle 1\,1\,1\rangle\{1\,1\,2\}$. For the first time step, a homogeneous initial dislocation density, $\rho_0$, is assumed throughout the grains and slip systems, corresponding to the yield stress following a standard relationship (Taylor, 1934):

$$\sigma_y = A\mu b\sqrt{\rho_0}, \tag{7}$$

where $\mu$ is the shear modulus, b is the Burgers vector, and the parameter $A$ is a constant that depends on the arrangement of dislocations (Widersich, 1964; Olivares et al., 1987; Schafler et al., 2005). Thus, for each slip system $\beta$, the initial dislocation density[1] on that slip system in each element would be taken as $\rho_o^{(\beta)} = \rho_o/24$. The parameter $A$ has been measured and theoretically calculated for various materials and is generally reported to be in the range 0.3–0.6 (Widersich, 1964; Schoeck and Frydman, 1972; Kassner, 1990; Orlová, 2004; Schafler et al., 2005; Gubicza et al., 2009). Here, a value of $A = 0.4$ was selected as a reasonable intermediate value.

The slip resistance for the $\alpha$th slip system, $g^{(\alpha)}$, is expressed as follows:

$$g^{(\alpha)} = A\mu b\sqrt{\sum_{\beta=1}^{NS} h_{\alpha\beta}\rho^{(\beta)}}, \tag{8}$$

where $\rho^{(\beta)}$ is the dislocation density for slip system $\beta$, and $h_{\alpha\beta} = \mathbf{n}^{(\alpha)} \cdot \xi^{(\beta)}$ are interaction cosines where $\mathbf{n}^{(\alpha)}$ and $\xi^{(\beta)}$ are the slip plane normal of $\alpha$th slip system and the dislocation line vector for slip system $\beta$, respectively. The geometric formulation of $h_{\alpha\beta}$ has been presented elsewhere (Lee et al., 2010). It is sufficient to know that and that there are no arbitrary constants – only the geometric information of the slip planes and dislocation line directions. To complete the constitutive equations for a single crystal, a standard phenomenological model of dislocation evolution is adopted (Kocks, 1976)

$$\rho^{(\alpha)} = \frac{1}{b}\left(\frac{\sqrt{\sum_{\beta}^{NS}\rho^{(\beta)}}}{\mathbf{k}_a} - \mathbf{k}_b\rho^{(\alpha)}\right)\cdot(\gamma^{(\alpha)}), \tag{9}$$

where, $k_a$ and $k_b$ are material parameters representing generation and annihilation of dislocations, respectively. $k_a$ is a dimensionless parameter while $k_b$ has units of meters. There are thus three fitting parameters for SCCE-D; $\rho_0$, $k_a$ and $k_b$, whereas the conventional PAN model requires four or more adjustable parameters.

### 2.2. Meso-scale simulation (MSS)

The novel MSS utilizes the slip activity and stress computed by the GSS in each element and redistributes the mobile part[2] of dislocation densities thus changing slip resistance at the next GSS time step. Dislocations interact elastically with the stress fields from the other dislocations and the external stress field. Thus, for $n$ discrete dislocations interacting, $n^2$ interactions would need to be computed to obtain the equilibrated spatial distribution of discrete dislocations. A typical range of dislocation densities is $10^{10}$–$10^{16}$ m$^{-2}$ (Dieter, 1976). It is the size of this problem that puts the direct treatment of individual dislocation in real materials beyond any realistic estimate of computational abilities.

Discrete dislocations were treated in a computationally more tractable way by lumping them within an element to form a superdislocation. A physical pile-up of $n$ discrete dislocations of Burgers vector $b$ is transformed mathematically into a statically equivalent one at large distances by lumping the dislocation content of one dislocation type (i.e. for one slip system) within a volume element into a single "superdislocation" with Burgers vector $B = nb$, where $n$ is the number of individual dislocations that were lumped. For each slip system type, the number of interacting superdislocations is equal to the number of finite elements in a grain ($N_E$). Using this method, the positions of each discrete dislocation are lost along with higher order moments of the dislocation content, but the dislocation density within a volume corresponding to the element size is maintained.

[1] The initial dislocation density, $\rho_0$, is a lumped value fit from the single-crystal yield stress via Eq. (7). It therefore includes all sources of slip resistance (solutes, Peierls stress, precipitates, etc.) treated as forest dislocation obstacles. In the future, it may prove necessary to treat this quantity as two values, one corresponding to real dislocations, and the other to other sources of internal slip resistance.

[2] The "mobile" part of the dislocation density is defined in a natural way within the model, as will be shown later.

A superdislocation for the $\alpha$th slip system has strength $B^{(\alpha)}$, equal to the discrete dislocation content in that volume on that slip system, as follows:

$$B^{(\alpha)} = n^{(\alpha)} b^{(\alpha)} = \frac{\rho^{(\alpha)} V^{(\alpha)} b^{(\alpha)}}{L^{(\alpha)}}, \tag{10}$$

where $n^{(\alpha)}$ is the number of discrete dislocations of Burgers vector $b^{(\alpha)}$ on the $\alpha$th slip system and $V^{(\alpha)}$ and $L^{(\alpha)}$ are the volume and characteristic length (in the direction parallel to the dislocation line vector) of the element. The characteristic length $L^{(\alpha)}$ is determined from a line parallel to the dislocation line passing through the center of the element and terminating at the element boundaries. The boundaries of the element are readily determined using the nature of the isoparametric finite elements employed (ABAQUS element C3D8).

The elastic force per unit length operating on the $i$th edge superdislocation segments caused by the stress field of $j$th superdislocation with parallel Burgers vectors of magnitude $B_1$ and $B_2$ in an isotropic elastic medium is as follows (Hirth and Lothe, 1969):

$$F_{ij} = \frac{F_{glide}}{dl_i} = \frac{\mu B_i B_j}{4\pi(1-\nu)} \frac{1}{(x_2 - x_1)} \left[ \frac{r_1}{(r_1^2 - r_2^2)} \right] [g_{11} + g_{22} - g_{12} - g_{21}], \tag{11}$$

where

$$G_{ij} = \frac{r_2^2}{R_{ij}} + (x_j + R_{ij}) \left( \frac{r_1^2 - r_2^2}{r_1^2 - r_2^2} \right),$$
$$R_{ij} = \sqrt{r_1^2 + r_2^2 + (y_i - x_j)^2} \quad i,j = 1,2.$$

Here, $r_1$, $r_2$ and $r_3$ are components of position vector $R_{ij}$ as shown in Fig. 3. Variables $x_i$ and $y_i$ denote relative termini of two dislocations with line direction, $\hat{\xi}_i$.

Grain boundaries act as barriers to dislocation motion at low temperature (Hirth and Lothe, 1969). The critical obstacle strength, $\tau_{obs}$, can be defined as the minimum stress operating on a single dislocation near a boundary required to activate transmission through or into the boundary (or to nucleate a dislocation in or on the other side of the boundary). $\tau_{obs}$ may depend on the orientation of the grain boundary (Shen et al., 1986, 1988), the misorientation of the grains (Livingston

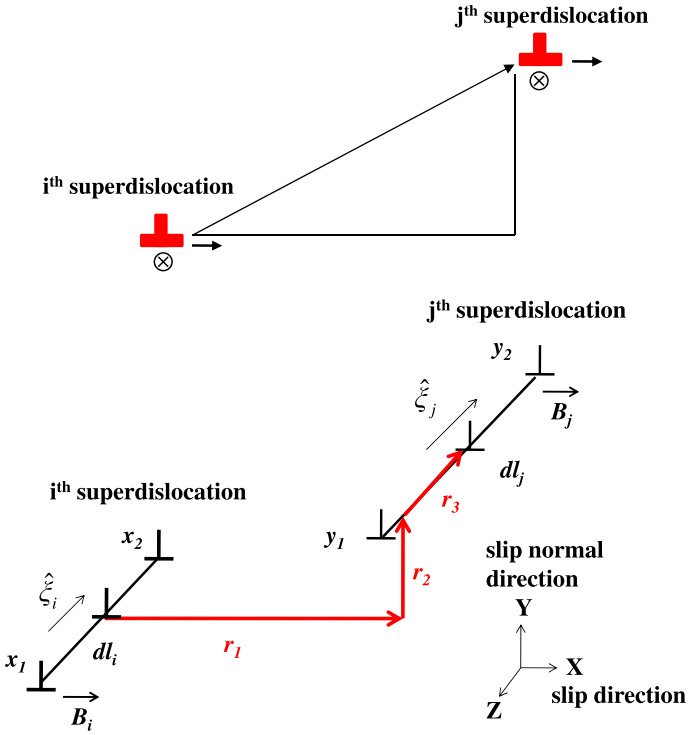


**Fig. 3.** The coordinate system and various quantities used for expressing the interaction force of superdislocation segment $j$ on superdislocation segment $i$ having parallel line directions $\xi$ and Burgers vectors $B$.

and Chalmers, 1957; Shen et al., 1986; De Messemaeker et al., 2004; Anderson and Shen, 2006), and the slip system geometry and stacking fault energies of the slip plane adjacent to the boundary (Anderson and Shen, 2006).

Livingston and Chalmers (1957) first proposed a slip criterion considering a geometry of slip systems in two adjacent grains and defined slip transmissivity, $N$, as follows:

$$N = (e_1 \cdot e_i)(g_1 \cdot g_i) + (e_1 \cdot g_i)(g_1 \cdot e_i), \tag{12}$$

where $e_1$ and $g_1$ are the slip plane normal and slip direction of the pile-up dislocations in the incoming plane, and $e_i$ and $e_i$ are the corresponding quantities in the adjacent grain. This criterion predicts that dislocations are most easily transmitted through the grain boundary if the slip transmissivity, $N$, has a maximum value. This criterion, however, does not consider the orientation of the grain boundary and failed to predict the observed emitted slip systems (Shen et al., 1986).

Shen et al. (1986) proposed a series of alternative slip transmission criteria (SWC criteria) that consider grain boundary orientations, applied stress or both. In particular, SWC 2nd criterion (Shen et al., 1986) considers boundary orientation and predicted emitted slip system relatively well without involving complicated calculation of local stresses. SWC 2nd criterion, adopted here for simplicity, is as follows:

$$N = (L_1 \cdot L_i) \times (g_1 \cdot g_i), \tag{13}$$

where $L_1$ and $L_i$ are the intersection lines between grain boundary and slip planes and $g_1$ and $g_i$ are the slip directions of incoming and emitted dislocations, respectively. For a given slip system on the incoming side of a boundary, the minimum value of $\tau_{obs}$ is chosen from the values computed for all of the allowed outgoing slip systems. The transmissivity ranges from 0 to 1 representing maximum and minimum obstacle stress, respectively.

Slip transmission criteria such as Eq. (13) can be reformulated to predict numerical values of the grain boundary obstacle stress in terms of an unknown maximum obstacle strength, $\tau^*$ (for the boundary/misorientation combination with lowest transmissivity)

$$\tau_{obs} = (1 - N)\tau^*, \tag{14}$$

where $\tau^*$ is the maximum grain boundary obstacle strength. Shen et al. (1986) calculated lower-bound obstacle strengths of 280–870 MPa for four grain boundaries from pile-up configuration as listed in Table 3. Using that data, $\tau^*$ is estimated to be 1.1 GPa, approximately five times the macroscopic yield stress (210 MPa for bulk yield stress of annealed 304 stainless steel).

MSS redistributes "mobile" dislocations among adjacent elements to enforce consistency with the plastic strain increment through Orowan's equation (Orowan, 1940) for slip system $\alpha$:

$$\dot{\gamma}^{(\alpha)} = \rho_m^{(\alpha)} b \cdot \dot{x}^{(\alpha)}, \tag{15}$$

where $\dot{\gamma}^{(\alpha)}$ is the plastic shear strain rate, $\rho_m^{(\alpha)}$ is the mobile dislocation density (i.e. that population of dislocations that moves through the element), $b$ is the Burgers vector, and $dx^{(\alpha)}$ is the characteristic length that dislocations moved along the slip plane $\alpha$. Eq. (15), along with Eqs. (16) and (17), below, defines the mobile dislocation content. That is, it represents the minimum, polar content required to obtain the required strain rate, consistent with the constitutive equation for a single crystal.

By assuming that all dislocations move the same distance, from one element to the adjacent element, dislocation densities required to accommodate the plastic strain increment obtained from the GSS can be calculated for each element as follows:

$$\dot{\rho}_{pass}^{(\alpha)} = \frac{1}{bl^{(\alpha)}} \dot{\gamma}^{(\alpha)}. \tag{16}$$

Here, $\dot{\rho}_{pass}^{(\alpha)}$ is the rate of dislocation density that passed through the element and $l^{(\alpha)}$ is the length of the element parallel to the slip plane $\alpha$. In order to obtain the net mobile dislocation density in each element, the net flux of dislocation density between two elements is obtained, as illustrated in Fig. 4:

$$\dot{\rho}_i^{(\alpha)} = \dot{\rho}_i^{(\alpha),in} - \dot{\rho}_i^{(\alpha),out}. \tag{17}$$

After the mobile dislocations are redistributed, the back stress is obtained by considering dislocation interactions within the same slip plane. In contrast to back stress formulations based on statistical models (Groma, 1997; Yefimov and van der Giessen, 2004) or strain gradient approaches (Evers et al., 2004), the two-scale model keeps track of dislocation densities

**Table 3**
Measured obstacle strength for 304 stainless steel (Shen et al., 1986) and calculated dislocation transmissivity factors for four grain boundaries.

| Boundary | $\tau_{obs}$ (MPa) | Transmissivity ($N$) |
|---|---|---|
| 1 | 380 | 0.588 |
| 2 | 280 | 0.915 |
| 3 | 870 | 0.472 |
| 4 | 400 | 0.785 |

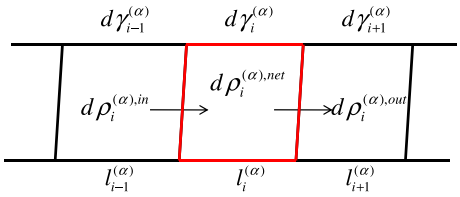


$$d\rho_i^{(\alpha),in} = \frac{d\gamma_{i-1}^{(\alpha)} + d\gamma_i^{(\alpha)}}{b(l_{i-1}^{(\alpha)} + l_i^{(\alpha)})}$$

$$d\rho_i^{(\alpha),out} = \frac{d\gamma_i^{(\alpha)} + d\gamma_{i+1}^{(\alpha)}}{b(l_i^{(\alpha)} + l_{i+1}^{(\alpha)})}$$

$$d\rho_i^{(\alpha),net} = d\rho_i^{(\alpha),in} - d\rho_i^{(\alpha),out}$$

**Fig. 4.** Redistribution of the mobile dislocation density from one element to adjacent elements.

(or, equivalently, the number of dislocations) for each element and slip system so that the back stress can be obtained explicitly without involving an arbitrary length scale. The back stress on the $i$th dislocation, $\tau_i^b$, can be represented as follows:

$$\tau_i^b = \frac{1}{b}\sum_{\substack{j=1 \\ j\neq i}}^{N} \mathbf{F_{ij}}, \tag{18}$$

where $\mathbf{F_{ij}}$ is computed using Eq. (11). The back stress and obstacle strength imposed by the grain boundary are incorporated in the slip system constitutive response, Eq. (6), for grain-interior elements as follows:

$$\dot{\gamma}^{(\alpha)} = \dot{\gamma}_0 \left( \left| \frac{\tau_{eff}^{(\alpha)}}{g^{(\alpha)}} \right| \right)^{1/m} sign\left(\tau_{eff}^{(\alpha)}\right), \tag{19}$$

where $\tau_{eff}^{(\alpha)} = (\tau^{(\alpha)} - \tau^{b(\alpha)})$. For grain boundary elements, the corresponding equations incorporate the boundary obstacle stress, $\tau_{obs}^{(\alpha)}$, as follows:

$$\tau_{eff}^{(\alpha)} > \tau_{obs}^{(\alpha)} \quad \dot{\gamma}^{(\alpha)} = \dot{\gamma}_0 \left( \left| \frac{\tau_{eff}^{(\alpha)} - \tau_{obs}^{(\alpha)}}{g^{(\alpha)}} \right| \right)^{1/m} sign\left(\tau_{eff}^{(\alpha)} - \tau_{obs}^{(\alpha)}\right), \tag{20}$$

$$\tau_{eff}^{(\alpha)} \leqslant \tau_{obs}^{(\alpha)} \quad \dot{\gamma}^{(\alpha)} = 0, \tag{21}$$

where $\tau_{obs}^{(\alpha)}$ is computed according to Eq. (14). Note that the obstacle stress is the stress that opposes the slip for the grain boundary elements, and therefore it cannot exceed $\tau_{eff}^{(\alpha)}$. That is, $\tau_{obs}^{(\alpha)}$ functions as a frictional stress and only attains its maximum value when dislocations are being transmitted.

### 2.3. Parametric test: A simple pile-up

A linear pile-up of collinear edge dislocations was simulated using the two-scale model for comparison with two equivalent solutions: (1) an analytical solution based on a continuous dislocation pile-up description and (2) a FE solution solving for internal equilibrium among superdislocations at the centers of the elements. The same number of dislocations is involved in each arrangement. For the two-surface model and FE model, a solid domain of 20 elements in the slip direction/Burgers vector direction had element dimensions of 50 μm (slip direction) × 20 μm × 20 μm. See the inset of Fig. 5 for the geometry of the problem.

For the two-scale model, at the right end of the specimen a free surface boundary condition is applied; at the left end an obstacle stress of 375 MPa must be exceeded before any slip takes place through the boundary. A constant shear stress of 110 MPa is applied such as to propel dislocations toward the grain boundary. Constitutive and initial parameters were chosen as follows: a constant slip resistance of 10 MPa (corresponding to a forest dislocation density on the slip plane of $1.6 \times 10^{12}$ m$^{-2}$), a strain rate sensitivity parameter of $m = 1$, and a reference shear rate, $\dot{\gamma}_0$, of 0.001/s. The value of $m$ has no effect on single-slip solutions. A value of $m = 1$ was chosen for numerical convenience. The initial dislocation density on the single active slip system was zero, and it increased according to the model until the obstacle stress was exceeded, which occurred when the corresponding total dislocation content in the specimen was $1.2 \times 10^4$ (i.e. an average dislocation density of $6 \times 10^{11}$ m$^{-2}$).

The analytical solution for a single, continuous pile-up against an obstacle under the influence shear stress $\sigma$ is as follows (Hirth and Lothe, 1969):

$$n(x) = \frac{2(1-\nu)\sigma}{\mu b}\left(\frac{l-x}{x}\right)^{\frac{1}{2}}, \tag{22}$$

where $\mu$ is the shear modulus, $\nu$ is Poisson's ratio and $b$ is the Burgers vector, respectively. This is for dislocations of infinite length in an infinite medium. Here, $n(x)dx$ is the number of dislocations located between $x$ and $x + dx$. The pile-up length, $l$, in

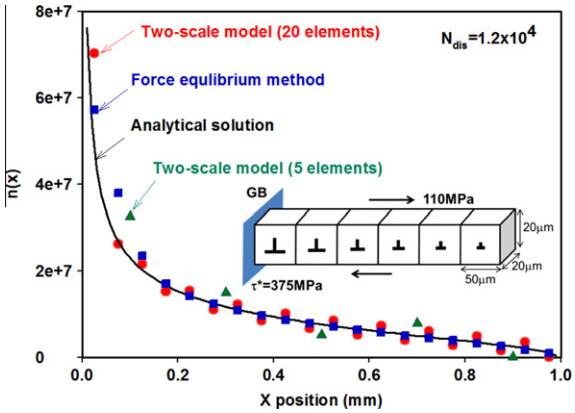


**Fig. 5.** Simulated number of dislocations per length for a simple pile-up computed according to an analytical solution, and two numerical schemes: (1) enforcing internal force equilibrium among lumped superdislocations (one per element), and (2) the two-scale model. The two-scale model results are shown for two meshes for the same domain ($1000 \times 20 \times 20$ μm): five elements and 20 elements.

Eq. (22) was determined using Eq. (2), for the total dislocation content, $n$ in Eq. (2), equals to the result for the two-scale model. This procedure ensures that the same dislocation content is subjected to the same applied stress for the comparison.

Note: The foregoing points to a conceptual problem with simple pile-ups in solid crystals. There is no connection between dislocation content in pile-ups to strain in the finite domain, nor is the number of pile-ups in a given section of boundary known. (Another way of thinking about it: for a specified number of dislocations in a given volume element, there is no way to distinguish whether this are arranged in one co-planar pile-up or that each dislocation is on a unique slip plane, i.e. that there is no pile-up.) For example, for the procedure used here to find the equal dislocation content for the single pile-up, it would have $1.2 \times 10^4$ dislocations in it, which for a co-planar arrangement and an applied stress of 110 MPa would have a tip stress (activating slip through the boundary obstacle stress of 375 MPa) of 132,000 MPa! Conversely, for an obstacle stress of 375 MPa and an applied stress of 110 MPa, a continuous single pile-up would have only 3.4 dislocations in it, and there would by necessity need to be 3500 of such pile-ups to match the dislocation density from the solid models. The original pile-up concept of Hall and Petch neatly avoids these conceptual difficulties by divorcing the pile-up content from strain and associating the pile-up length with the grain size, or an unknown fraction thereof, thus introducing an arbitrary length scale.

The FE solution enforces internal equilibrium among superdislocations at the centers of the elements. Each such superdislocation experiences forces from the fields of the other superdislocations and from the applied stress field. Equilibrium requires that the sum of these forces be zero for all superdislocations. Ignoring lattice friction stresses or other local constraints to dislocation motion, the defect equilibrium equation condition may be expressed as follows:

$$F_i = \sum_j F_{ij} + (B_i \cdot \sigma) \times \xi_i = 0, \tag{23}$$

where $F_{ij}$ represents the elastic force per unit length operating on the $i$th superdislocation caused by the stress field of $j$th superdislocation (shown explicitly in Eq. (11)) and the second term is the well-known Peach–Koehler formula (Hirth and Lothe, 1969) representing the force exerted by the applied stress tensor on $i$th superdislocation having Burgers vector $B_i$ and line direction $\xi_i$. Solution of Eq. (23) provides the magnitude of the Burgers vector of the superdislocation, $B_i$, located at the center of each element, subject to the constraint that the number of equivalent dislocations is $1.2 \times 10^4$. The obstacle stress is again interpreted as that stress needed to push a single dislocation of Burgers vector $b$ through the boundary, i.e. 375 MPa.

Fig. 5 compares calculated dislocation distributions for the three kinds of pile-up solutions, and for two mesh sizes for the two-scale model (5 and 20 elements). All four are consistent, within the approximation of the numerical treatments. The numerical solutions are mesh-independent except for the inherently better resolution of gradients offered by finer elements. The analytical solution and force equilibrium method require as inputs only the total number of dislocations in the domain and the applied stress to obtain the spatial distribution of dislocations. Conversely, the two-scale model solution requires both the stress and strain of each element.

Note: The FE internal equilibration scheme suggests an alternate way to construct a two-scale model, i.e. by redistributing total dislocation content (as determined by Eq. (9)) to enforce defect internal equilibrium on each slip system in a polycrystal, and enforcing an obstacle stress using Eqs. (13) and (14). This scheme was in fact formulated (Lim et al., 2010), it does predict the Hall–Petch effect and it automatically reproduces simple pile-up solutions. However, it neglects the

**Table 4**
Chemical composition of minimum alloy steel and Fe-3% Si (wt.%).

| | Minimum alloy steel | Fe-3% Si |
|---|---|---|
| C | 0.001 | 0.004 |
| Mn | 0.13 | 0.09 |
| P | 0.006 | 0.01 |
| S | 0.005 | 0.025 |
| Si | 0.004 | 2.95 |
| Cu | 0.023 | 0.02 |
| Ni | 0.007 | 0.01 |
| Cr | 0.014 | – |
| Mo | 0.003 | – |
| Sn | 0.002 | – |
| Al | 0.038 | 0.03 |
| Ti | 0.001 | – |
| N | 0.003 | 0.015 |
| Nb | 0.001 | – |

crucial relationship between the plastic strain and the required movement of dislocation densities to attain that strain. Hall–Petch slopes predicted by this model were a factor of ~30 smaller than measured ones (Lim et al., 2010).

## 3. Experimental procedures

Three kinds of experiments to be compared with the two-scale simulation predictions were conducted: (1) stress–strain curves for minimum alloy steel multi-crystals (9–39 grains), (2) Hall–Petch slopes, and (3) lattice curvature distribution for a Fe-3% Si multi-crystal. Minimum alloy steel samples were heat treated to obtain various grain sizes to measure the Hall–Petch slope and the largest-grained tensile specimens were used to compare the measured stress–strain response of multi-crystals (9–39 grains) to the two-scale simulation. Crystal orientations of a columnar-grained Fe-3% Si tensile specimen were obtained using OIM (Orientation Imaging Microscopy) before and after the deformation to compare the measured and simulated lattice curvatures.

### 3.1. Materials

Minimum alloy steel (essentially pure iron with Mn for control of hot shortness[3]) provided by Severstal N/A has advantages that a wide range of grain sizes is obtainable, it has good ductility, and, a large Hall–Petch slope (0.88 $MN/m^{3/2}$). As provided, in sheet form with the thickness of 2.1 mm, the initial grain size of minimum alloy steel was 60 μm. Heat treatment was carried out to obtain three other grain sizes. Grain sizes of 140 μm and 620 μm were obtained by the heat treatment at 1000 °C and 1250 °C for 5 h in a vacuum furnace, respectively. The largest grain size of 1350 μm was obtained by strain annealing (Keh, 1961); initially heat treated at 1000 °C for an hour in a vacuum furnace, strained to 2.5% and then reheated at 1250 °C for 10 h.

Coarse-grained Fe-3% Si with only single grain through the thickness is fabricated and provided by AK Steel in sheet form with the thickness of approximately 0.3 mm. The material is generally hot rolled, cold worked, annealed, decarburized, coated then box annealed. Material parameters for single crystal constitutive equations for Fe-3% Si are reasonably well established (Wagoner et al., 1998) and has an advantage that a wide range of grain sizes, from 10 μm to 30 mm, can be readily obtained but the sample with grains larger than 2 mm showed poor ductility (<10%). The chemical composition of minimum alloy steel and Fe-3% Si is listed Table 4.

### 3.2. Tensile tests

Three sets of tensile tests were performed with different strain rates, specimen dimensions, and procedures as listed below:

- Special tensile specimens (Fig. 6) having 9–39 grains in the reduced section were water-jet machined from heat-treated minimum alloy steel. The first two specimen types have reduced section width of 1 mm and 2 mm and the original sample thickness of 2.1 mm. The specimen type III has the same sample dimensions as type II but the sheet was cold rolled to a thickness of 0.4 mm (19% of the original thickness). Tensile tests were performed at a nominal strain rate of $\sim 5 \times 10^{-4}\,s^{-1}$.
- Sub-sized ASTM E8 tensile specimens (gage area 25.4 mm in length and 6.35 mm in width) were machined from minimum alloy steel that had been heat treated to obtain four grain sizes: 60, 140, 620 and 1350 μm. The tensile tests were performed at a nominal strain rate of $\sim 5 \times 10^{-4}\,s^{-1}$.

[3] "Hot shortness" is cracking that occurs during the hot rolling of steels. It can be avoided by additions of Mn.

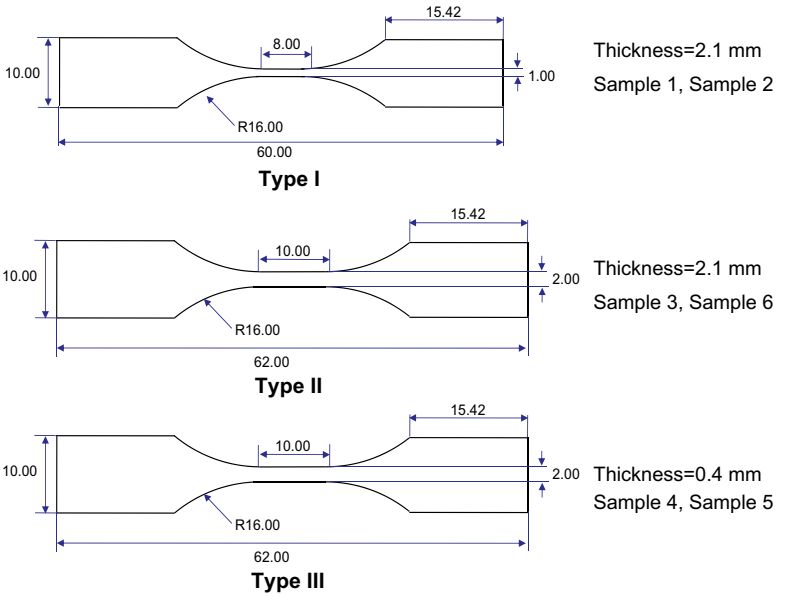


**Fig. 6.** Dimensions of three tensile sample types used for testing of multi-crystal minimum alloy steel (unit: mm).

- Standard ASTM E8 tensile specimens (gage region 50.8 mm in length and 12.7 mm in width) were water-jet machined from columnar grained Fe-3% Si. These were deformed to 8% strain at a nominal strain rate of $\sim 1.3 \times 10^{-4}\ s^{-1}$.

All tensile tests were performed using an MTS-810 testing machine with 100 kN hydraulic grips, at room temperature. The extension of the reduced section was measured with a laser extensometer, Epsilon Tech Corp. LE-05.

### 3.3. EBSD characterization and lattice curvature calculation

Minimum alloy steel and Fe-3% Si tensile specimens were polished using diamond paste down to 1 μm and colloidal silica (50 μm). Crystal orientations of tensile specimens were then measured using OIM and a FEI-Philips XL-30 SFEG equipped with a DigiCam system, with pattern collection controlled by TSL OIM DC 4.6 software. Initial crystal orientations were scanned with an accelerating voltage of 20 kV at step sizes of 35 μm and 10 μm for minimum alloy steel and Fe-3% Si tensile specimens, respectively. For the Fe-3% Si tensile sample, a step size of 1 μm was used to scan the deformed specimen over a smaller region of interest having four grains and two triple junctions (Fig. 7).

Lattice curvature, $\kappa_{ij}$, represents the change in orientation of the crystal lattice with respect to the change in point of measurement as follows (Nye, 1953; Sun et al., 2000):

$$\kappa_{ij} = \frac{d\phi_i}{dx_j}, \tag{24}$$

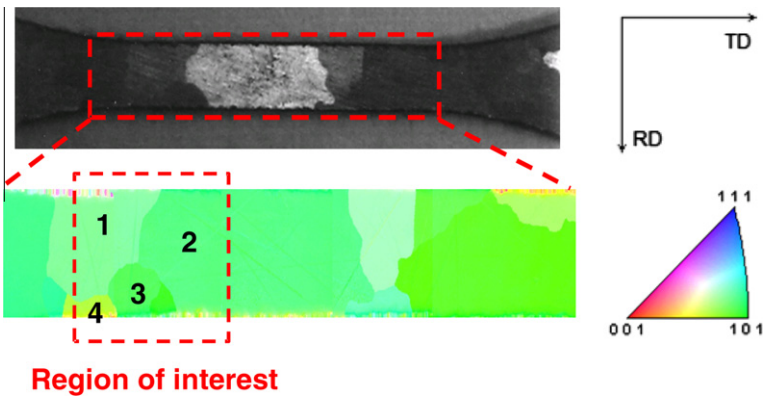


**Fig. 7.** Surface image (optical microscope) and inverse pole figure (OIM) for an Fe-3% Si tensile sample.

where, $d\phi_i$ is the change in orientation and $dx_j$ is the change in position of the test point. The diagonal components of $\kappa_{ij}$ represent twisting of the lattice about the $x_i$ axes, and the off-diagonal terms represent bending of the $x_i$ plane, about the $x_j$ direction. Under the assumption that the mean curvature $\bar{\kappa}$ can be expressed as an averaged value of six in-plane components (Adams and Field, 1992; Sun et al., 2000; El-Dasher et al., 2003),

$$\bar{\kappa} \cong \frac{1}{6}\sum_{i=1}^{3}\sum_{j=1}^{2}|\kappa_{ij}| = \frac{1}{6}\sum_{i=1}^{3}\sum_{j=1}^{2}\left|\frac{d\phi_i}{dx_j}\right|. \tag{25}$$

In order to obtain mean curvature, $\bar{\kappa}$, from the two-scale model, the following equations relating the dislocation tensor to the lattice curvature were used (Nye, 1953; Sun et al., 2000; Hartley, 2003):

$$\kappa_{ij} = -\alpha_{ij} + \frac{1}{2}\delta_{ij}\alpha_{kk} - e_{ijk}\varepsilon^{e}_{jk,l}, \tag{26}$$

where $e_{ijk}$ denotes components of the permutation tensor and $\alpha_{ij}$ is a dislocation tensor that can be represented as follows (Nye, 1953):

$$\alpha_{ij} = \sum^{NS}\rho^{(s)}b_i^{(s)}z_j^{(s)}, \tag{27}$$

where $\rho^{(s)}$ denotes the density of dislocation character (i.e. screw, edge or mixed) $s$, $b^{(s)}$ is the Burgers vector of that type, and $z^{(s)}$ is the line direction of the dislocation type. Since only edge dislocations are considered in the current two-scale model, the dyadic in Eq. (27) is uniquely determined with a geometric definition of dislocation on each slip system. Using Eqs. (25)–(27), the average lattice curvatures, $\bar{\kappa}$, are calculated from the lattice misorientation and polar dislocation distribution inside the grains obtained from the two-scale simulation.

## 4. Results

In order to compare the accuracy of the two-scale model to the other models (CP-FEM and Taylor models with SCCE-D and PAN constitutive equations), adjustable parameters were fit to reproduce the measured stress–strain response of multi-crystal minimum alloy steel tensile specimens having 39 grains. Then each model was used to predict the stress–strain response for other specimens having 9–34 grains. Using best-fit parameters, the Hall–Petch slope for 2-D and 3-D arrays of cubic grain assemblies having 4–125 grains were predicted. In addition, measured and simulated lattice curvatures of 8% strained Fe-3% Si sample were compared.

### 4.1. Multi-crystal stress–strain response

Fig. 8 show OIM grain maps and their crystal orientations (listed in Appendix A) within the reduced sections of six minimum alloy steel tensile specimens. Bitmap data for each specimen's grain map from the OIM measurements was utilized to distinguish the grains within specimens. The neck region was meshed with 8671 regular linear brick element (C3D8), superposed on the image. The size of the element was chosen to be smaller than the OIM measurement step size.

The following models were then fit to the stress–strain response for Sample 6 (Fig. 9), having the largest number of grains (39 grains), then used to predict the stress–strain response for specimens 1–5.

- Two-scale model – as introduced above: CP-FEM with a meso-scale simulation (MSS) at each time step to update dislocation densities used in the SCCE-D constitutive model (Lee et al., 2010).
- CP-FEM/ SCCE-D – the same finite element procedure for each multi-crystal, but using the SCCE-D constitutive model (Lee et al., 2010) without updating dislocation densities using the meso-scale simulation (MSS).
- CP-FEM/ PAN – the same finite element procedure for each multi-crystal, but using PAN constitutive equations (Peirce et al., 1983) to describe the singe-crystal continuum response.
- Taylor/ SCCE-D – each grain is treated as a single element of equal volume having a crystal orientation. The macroscopic mechanical response is computed using texture-type methods (Dawson et al., 2003) with the SCCE-D constitutive model.
- Taylor/ PAN – same as for Taylor/ SCCE-D, except the constitutive continuum model is of the PAN (Peirce et al., 1983) form.

This procedure is consistent with typical texture analysis procedures, where single crystal properties are inferred from polycrystal tensile tests. Best-fit parameters, anisotropic elastic constants and shear modulus for minimum alloy steel used for the simulation are shown in Tables 5 and 6. SCCE-D and PAN models utilize three and four fitting parameters, respectively; For PAN, $h_0$ affects the initial hardening rate, $g_s$ determines the final saturated value of stress, $g_0$ determines initial yield and $a$ affects the shape of the stress–strain curve (Kalidindi et al., 1992). For SCCE-D, $\rho_0$, $k_a$, and $k_b$ determines the yield stress and the shape of the flow curve, respectively. Detailed procedures used to obtain these best-fit parameters are described in the previous work (Lee et al., 2010).

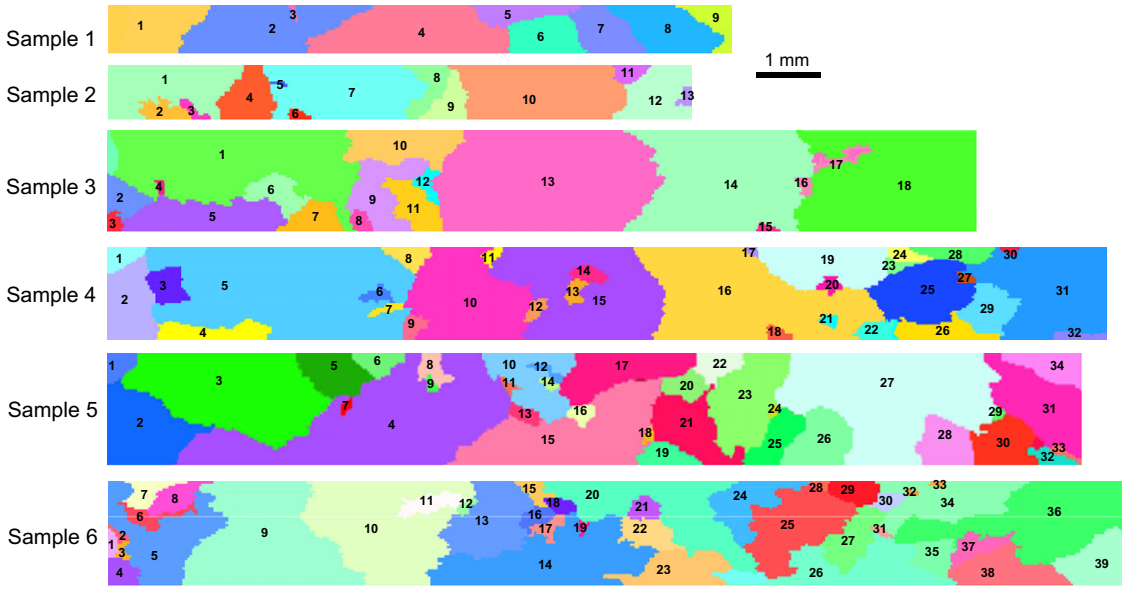


**Fig. 8.** Orientation imaging microscopy (OIM) grain map for reduced sections of six tensile specimens of minimum alloy steel. The colors are only for contrast. The crystal orientations for each numbered grain appear in Appendix A. (For interpretation of the references to colour in this figure legend, the reader is referred to the web version of this article.)

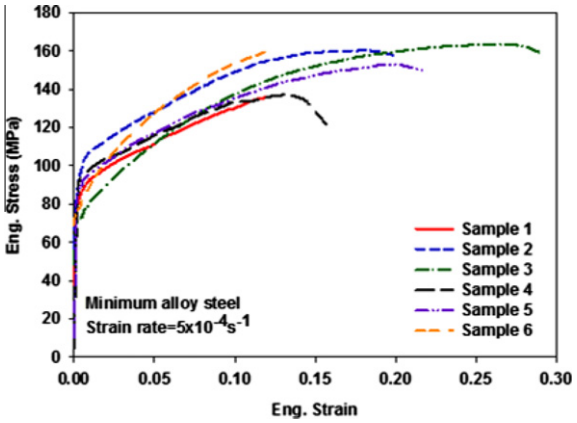


**Fig. 9.** Measured engineering stress–strain response for the six tensile samples of minimum alloy steel shown in Fig. 8.

**Table 5**
Shear modulus and anisotropic elasticity constants of iron (Hirth and Lothe, 1969) (unit: GPa).

| $\mu$ | $C_{11}$ | $C_{12}$ | $C_{44}$ |
|---|---|---|---|
| 80 | 242 | 150 | 112 |

**Table 6**
Best-fit parameters and standard errors of fit for various models fit to the stress–strain curve for Sample 6 of minimum alloy steel having 39 grains.

| Parameters | Two-Scale SCCE-D | CP-FEM SCCE-D | Taylor SCCE-D | Parameters | CP-FEM PAN | Taylor PAN |
|---|---|---|---|---|---|---|
| $\rho_0$ ($m^{-2}$) | $9.4 \times 10^{11}$ | $1.1 \times 10^{12}$ | $1.2 \times 10^{12}$ | $h_0$ (MPa) | 423 | 402 |
| $k_a$ | 63 | 26 | 16 | $g_s$ (MPa) | 162 | 240 |
| $k_b$ (m) | 7b | 15b | 25b | $g_0$ (MPa) | 38 | 40 |
| | | | | $a$ | 2 | 2 |
| Std. err. fit (MPa, (%)) | 1.1(0.8) | 1.0 (0.7) | 0.9 (0.7) | Std. err. fit (MPa, (%)) | 1.1 (0.8) | 2.3 (1.7) |

All models reproduced the measured stress–strain curve accurately, having standard errors of fit as shown in Fig. 10(a) and Table 6. Best-fit parameters for each model were then used to predict the mechanical response of the remaining five specimens having 9–34 grains. Predicted hardening curves using the best-fit parameters are shown in Fig. 10(b)–(f). Hardening curves were obtained by subtracting the yield stress (0.2% offset) from the total flow stress for each model.

Table 7 compares average standard deviations between predicted and measured hardening curves for each model. The averaged standard deviation between measurement and prediction is approximately three times larger for the CP-FEM model adopting PAN single crystal constitutive equations than for the two-scale model (16.6 MPa vs. 5.6 MPa, respectively). In accordance with similar tests for single crystals (Lee et al., 2010), the two-scale model adopting SCCE-D agrees better with measurements compared to the CP-FEM model with PAN single-crystal constitutive equations in spite of having fewer

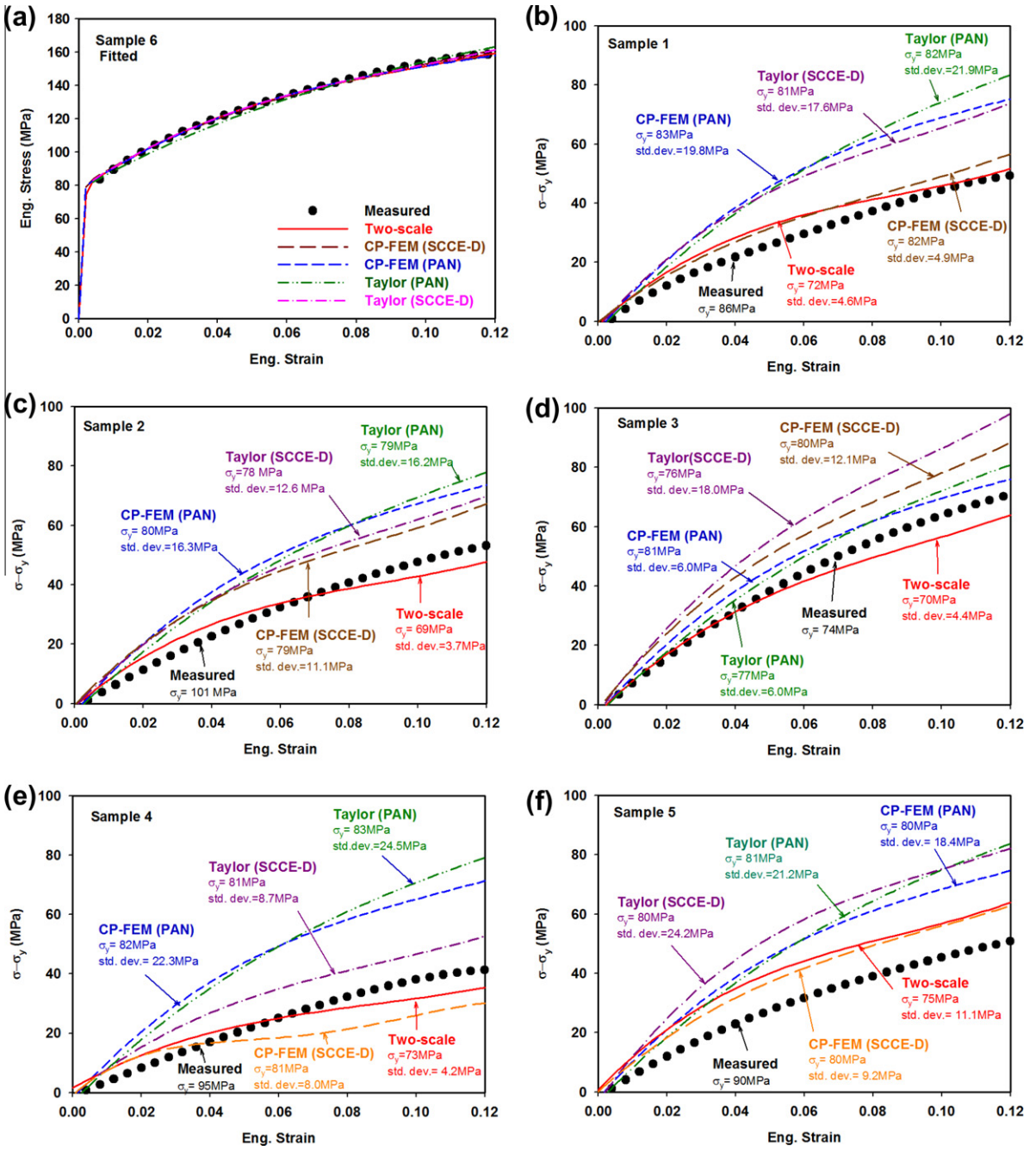


**Fig. 10.** Comparison of measured and predicted strain hardening for the five multi-crystals shown in Fig. 8 (Fig. 10(b)–(f)). The parameters for the constitutive models were fit by least-squares to the stress–strain data for Sample 6, Fig. 10(a).

**Table 7**
Standard deviations between predicted and measured stresses from 0% to 10% strain (unit: MPa).

| Samples | # of grains | Standard deviations (MPa) | | | | |
|---|---|---|---|---|---|---|
| | | Two-scale SCCE-D | CP-FEM SCCE-D | CP-FEM PAN | Taylor SCCE-D | Taylor PAN |
| Sample 1 | 9 | 4.6 | 4.9 | 19.8 | 18.6 | 22.6 |
| Sample 2 | 13 | 3.7 | 11.1 | 16.3 | 13.6 | 16.8 |
| Sample 3 | 18 | 4.4 | 12.1 | 6.0 | 19.1 | 6.6 |
| Sample 4 | 32 | 4.2 | 8.0 | 22.3 | 9.5 | 25.1 |
| Sample 5 | 34 | 11.1 | 9.2 | 18.4 | 25.3 | 21.8 |
| Average | | 5.6 | 9.1 | 16.6 | 17.2 | 18.6 |

arbitrary parameters. Taylor models, whether adopting PAN or SCCE-D showed larger standard deviations than either the two-scale model or CP-FEM models.

The likely source of error for the CP-FEM PAN model and Taylor models lies in ignoring the role of grain boundaries except as an integral part of the single-crystal constitutive equation. Fig. 10(b)–(f) illustrate that these models tend to over-predict hardening of the multi-crystals. Recall that all models were fit to multi-crystals with the most number of grains and the stress–strain response was then predicted for samples with fewer grains. This over-prediction implies that the best-fit parameters obtained from Sample 6, which is the most polycrystal-like, do not represent well the hardening behavior for samples with fewer grains. This is in agreement with similar comparisons for single crystals (Lee et al., 2010). The averaged standard deviation for prediction using GSS alone is 9.1 MPa, Table 7, larger than the full two-scale model. This indicates that the back stress and redistribution of mobile dislocations within the MSS increases accuracy of the prediction over a range of grain configurations.

Despite the two-scale model showing good agreement for hardening of multi-crystals, both models failed to predict the measured yield stresses accurately using the current prediction scheme. Values of $\rho_0$ and $g_0$ for SCCE-D and SCCE-T were determined from the initial yield stress of Sample 6 using Eq. (7). The predicted yield stresses for the other specimens were 70–76 MPa and 81–84 MPa for the two-scale model and CP-FEM PAN model, respectively, while the measured yield stress ranged from 63 to 96 MPa. This deviation may be related to altered initial dislocation densities or defects created during specimen preparation and polishing. Another possibility is the non-Schmid nature of slip in BCC crystals that may affect the initial yield stress of the multi-crystal tensile samples (Christian and Vitek, 1970; Duesbery and Richardson, 1991; Vitek, 1992; Vitek et al., 2004).

### 4.2. Hall–Petch slopes

Figs. 11 and 12 show stress–strain responses for minimum alloy steels with various grain sizes and Hall–Petch slopes at the yield stress and at 10% strain, respectively. ASTM E8 sub-sized specimens and six multi-crystal tensile specimens were used to obtain Fig. 12. Uniaxial tension of 2D and 3D array of grain assemblies having 4–64 and 8–125 grains with four random crystal orientations were simulated using the two-scale model as shown in Fig. 13. A total of 8000 solid elements (C3D8) were used ($40 \times 40 \times 5$ for 2D and $20 \times 20 \times 20$ for 3D) with the dimensions of 1 mm×1 mm×0.1 mm and 1 mm×1 mm×1 mm for 2D and 3D case, respectively. Best-fit material parameters for minimum alloy steel obtained from the previous section (Table 6) and $\tau^*$ of 375 MPa (~5 times the yield stress (Shen et al., 1986)) were used.

While the Hall–Petch slopes presented in Fig. 14 from the two-scale model and experiments fall within the combined scatter, the differences in yield stress are remarkable, particularly at small grain sizes. This can be understood as follows.

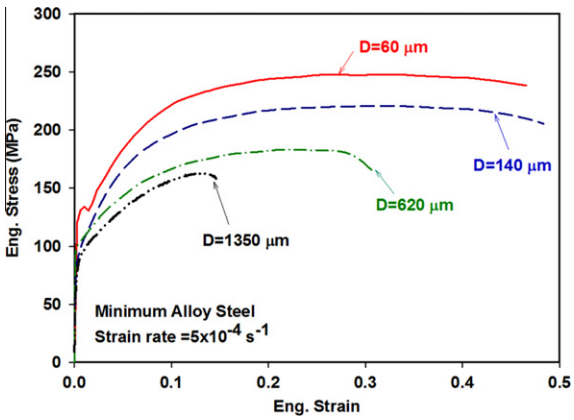


**Fig. 11.** Tensile stress–strain curves for minimum alloy steels with four grain sizes.

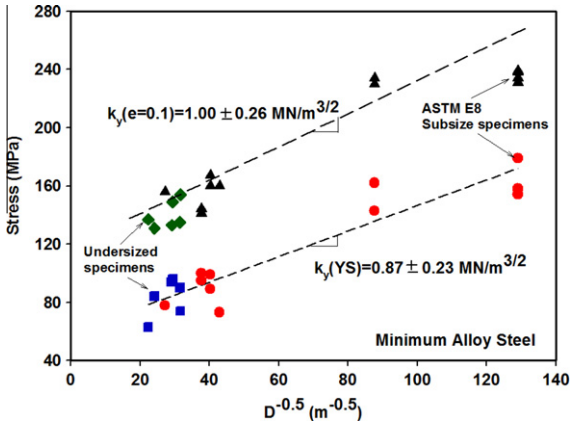


**Fig. 12.** Measured Hall–Petch slopes for minimum alloy steel at yield and for an engineering strain of 0.1.

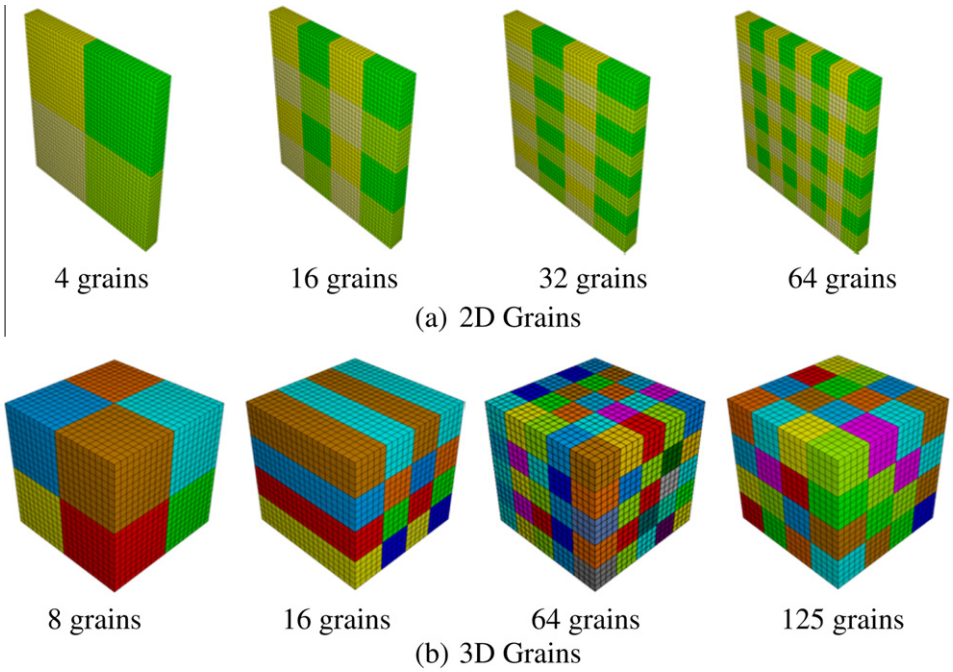


**Fig. 13.** Configurations of idealized multi-grain samples with various numbers and sizes of the grains: (a) 2D samples having 4–64 grains and (b) 3D samples having 8–125 grains. The colors correspond to crystal orientation; each 2-D or 3-D sample maintains the same texture as the grain size and number is varied. (For interpretation of the references to colour in this figure legend, the reader is referred to the web version of this article.)

Except for the Hall–Petch equation, there is no fundamental reason to expect that the plot will be linear, particularly at the extremes of grain size. In fact, it is well-known that the slope changes for very small grain sizes, and may well do so at very large grain sizes. It is interesting to note that the two curves from the two-scale model and the line from the experiments converge at a single point, albeit at a point outside of the graph. This suggests that the single-crystal properties are consistent (which they are known to be for the two kinds of simulation), but also that the lines become nonlinear at very large grain sizes. Another way to look at the question: the difference in slopes, which is what has been focused on in this context, leads automatically to greatly differing flow stresses for small grain sizes because the simulations use common properties for the single crystals (see Fig. 15).

Fig. 14 compares the measured Hall–Petch slope to that simulated using the two-scale model for 2D and 3D grain assemblies. The force equilibrium method presented in Fig. 14 refers to a method described in Section 2.3 that utilizes Eq. (23) to obtain dislocation densities along the slip plane. For 2D grain assemblies, the force equilibrium model showed negligible size dependence ($k_y = 0.03 \pm 0.01$ MN/m$^{3/2}$), whereas the two-scale model predicted the magnitude of the Hall–Petch slope ($k_y = 1.2 \pm 0.3$ MN/m$^{3/2}$), within the combined scatter of the measurements and simulations. The Hall–Petch model,

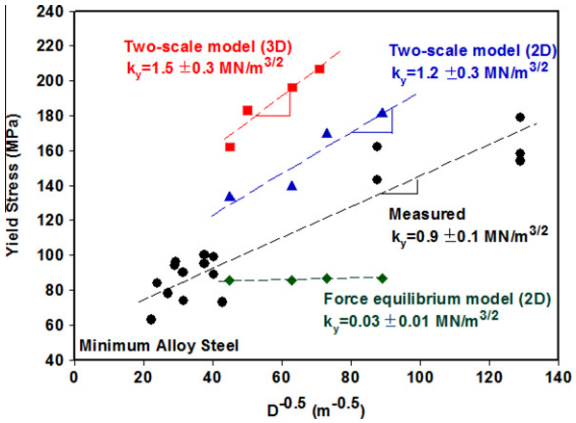


**Fig. 14.** Comparison of yield stress and its dependence on grain size from measurements and two-scale simulations using 2-D and 3-D arrays shown in Fig. 13.

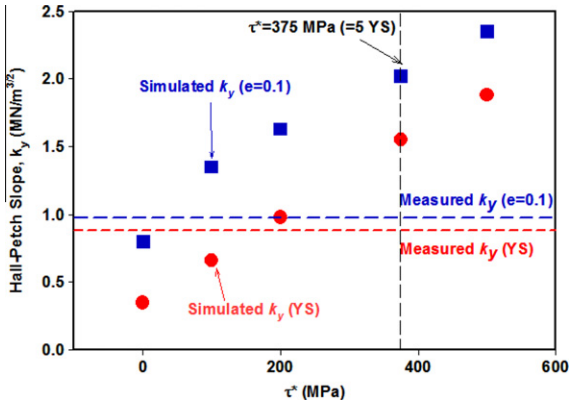


**Fig. 15.** Effect of the maximum obstacle stress, $\tau^*$, on two-scale simulated Hall–Petch slopes for the 3D grain arrays shown in Fig. 13.

Eq. (3), predicts a Hall–Petch slope of 0.18 MN/m$^{3/2}$, smaller than that measured by a factor of 5. For the 3D case, the two-scale model over-predicted the Hall–Petch slope by a factor of approximately 1.5 when $\tau^*$ of 375 MPa was used.

The predictions show that equivalent slopes for higher strains are higher, in agreement with measurements, although the predicted increase is much larger. The two-scale model predicted higher Hall–Petch slopes at larger strains through increased strain hardening for smaller grain sizes. However, predicted Hall–Petch slope at 10% strain was larger than that for the measured by a factor of 2–3 as shown in Table 8. This deviation was more significant for the 2D case, possibly due to an unrealistic surface to volume ratio compared to real polycrystal samples.

The parameters inherent in the two-scale model are either well-known and standard, are readily determined, or have little effect on the model predictions. Simulations were performed to probe the sensitivity of the Hall–Petch slope by changing each parameter by factors of ½ and 2. The change of Hall–Petch slope with the various parameter changes are as follows: $\tau^*$: ±80%, $\rho_o$: ±15%, all others ($k_a$, $k_b$, $m$, $\dot{\gamma}_0$ and $A$): maximum of 3%. Thus, $\tau^*$ is the critical parameter required to predict the Hall–Petch slope accurately. Fig. 15 shows the effect of $\tau^*$ on the Hall–Petch slope for 3D grain assemblies. In order to obtain the measured Hall–Petch slope of 0.9 MN/m$^{3/2}$ for 3-D simulations, a $\tau^*$ of 150–200 MPa or 2–3 times the yield stress would be required for minimum alloy steel.

**Table 8**
Measured and simulated Hall–Petch slopes ($k_y$) based on the yield stress and at strains of 5% and 10%.

| | Measured $k_y$ (MN/m$^{3/2}$) | Simulated $k_y$ (MN/m$^{3/2}$) | |
|---|---|---|---|
| | | 2D | 3D |
| Yield | 0.9 ± 0.1 | 1.2 ± 0.3 | 1.5 ± 0.3 |
| $e$ = 0.05 | 0.9 ± 0.1 | 2.4 ± 0.4 | 1.9 ± 0.3 |
| $e$ = 0.10 | 1.0 ± 0.1 | 2.9 ± 0.4 | 2.0 ± 0.3 |

### 4.3. Lattice curvature

Columnar-grained Fe-3% Si was used to compare the measured and simulated lattice curvature after deformation. Fig. 7 shows the region of interest (represented in dotted line) with four grains and two triple junctions and their initial Bunge's Euler angles for the four grains are listed in Table 9. From the initial grain map, the region of interest is meshed with 9600 elements (C3D8) and measured stress–strain curve is fitted using the two-scale model, similar to procedure for minimum alloy steel samples. Best-fit parameters for Fe-3% Si sample are as follows: $\rho_0 = 7 \times 10^{12}$ m$^{-2}$, $k_a = 98$ and $k_b = 8$b.

Fig. 16(a) and (b) show inverse pole figure and surface image of deformed Fe-3% Si after 8% strain, respectively. Fig. 16(d) shows the first example of simulated lattice curvature for a Fe-3% Si specimen after 8% strain. As shown in this figure, high curvatures are developed near the grain boundaries and near the two triple junctions with predicted curvature distribution confirmed by the measurements.

Note that high lattice curvatures were measured near the specimen edges, presumably related to surface irregularities and polishing artifacts. Excluding the high lattice curvatures measured near the specimen edges (i.e. by using only the area defined by the dotted line in Fig. 16(c)), the difference in maximum magnitude of curvatures is within 4%: $9.2 \times 10^{-3}$ rad/mm for the prediction using the two-scale model and $9.5 \times 10^{-3}$ rad/mm for the measurement. The two-scale model accurately predicted maximum lattice curvature and notably low lattice curvature at some grain boundaries, i.e. the vertical boundary in Fig. 16(c). On the other hand, the measured averaged lattice curvature was $5.8 \times 10^{-4}$ rad/mm while the simulated value using the two-scale model smaller by a factor of 8, $7.3 \times 10^{-5}$ rad/mm. This discrepancy may be related to the

**Table 9**
Initial grain orientations for four grains in the region of interest in the form of Bunge's Euler angles (°).

| Grain | $\varphi_1$ | $\Phi$ | $\varphi_2$ |
|---|---|---|---|
| 1 | 61 | 38 | 282 |
| 2 | 266 | 41 | 81 |
| 3 | 74 | 41 | 265 |
| 4 | 248 | 30 | 88 |

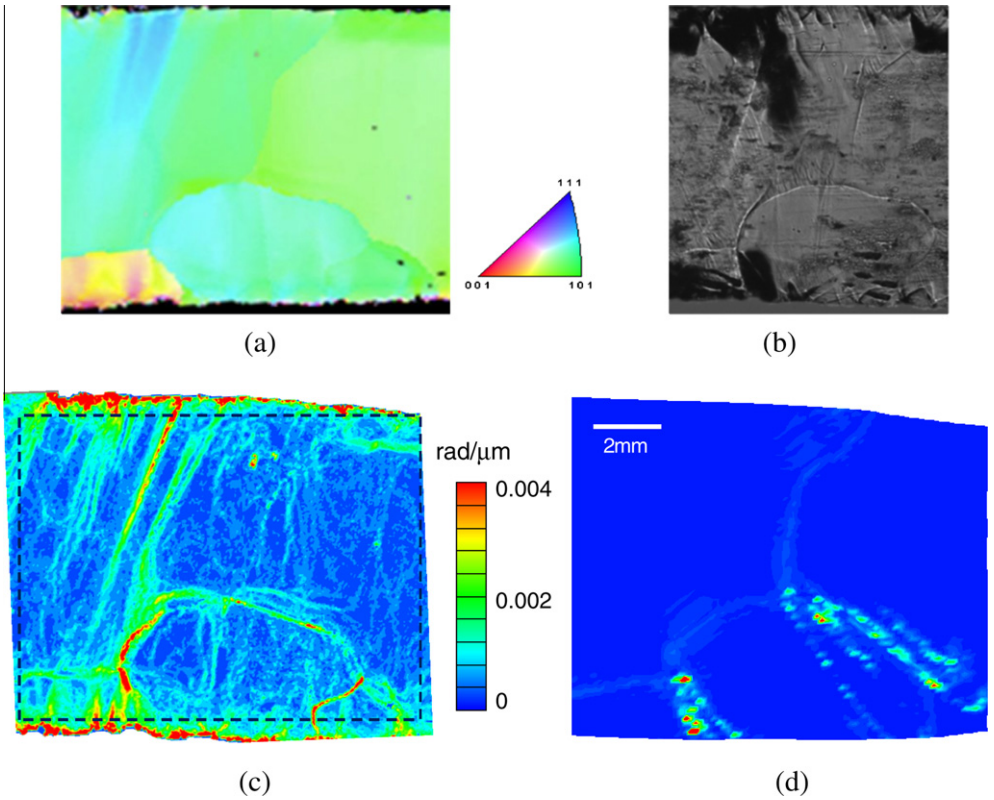


**Fig. 16.** Images of a section of an Fe-3% Si tensile specimen images after deformation to 8% strain: (a) inverse pole figure, (b) optical surface image, (c) color contour showing measured lattice curvature, and (d) two-scale simulated lattice curvature. (For interpretation of the references to colour in this figure legend, the reader is referred to the web version of this article.)

initial lattice curvature before the deformation and the trapping of dislocations within the sample as deformation proceeds. The two-scale model utilizes average grain orientations for each grain so that small differences in the orientation of the crystal lattice within the grain (i.e. from cell walls) are neglected.

## 5. Discussion

Several simulations were conducted to reveal predictions of the two-scale model to minimum alloy steel. Uniaxial tension of a grain-within-a-grain specimen was simulated to predict the evolution of dislocation densities. Reverse loading was simulated to observe the predicted Bauschinger effect for 16-grain samples.

### 5.1. Evolution of dislocation densities

A rectangular tensile sample with an embedded cylindrical grain was constructed as shown in Fig. 17(a). The crystal orientation of the cylindrical grain is misoriented by 45° relative to the rectangular grain. Uniaxial tension was applied and deformation to 10% strain was accomplished. The von Mises stress distribution is shown in the right figure of Fig. 17(a) while Fig. 17(b) shows the evolution of total dislocation density throughout the bicrystal. The dislocation density increases rapidly at the grain boundary. At 10% strain overall, the initial dislocation density of $9.4 \times 10^{11}$ m$^{-2}$ has increased to an average of $6.9 \times 10^{12}$ m$^{-2}$, with a maximum near the grain boundary of $3.4 \times 10^{13}$ m$^{-2}$. Fig. 17(c) shows the partitioning of dislocation density on 2 slip systems at 10% strain. The two slip systems, $(\bar{2}1\bar{1})[\bar{1}\bar{1}1]$ and $(1\bar{1}2)[\bar{1}11]$, represent the most active ones, producing the highest dislocation densities at an overall strain of 10%.

In order to assess the effect of grain orientations on the evolution of dislocation densities, the simulation was repeated but with the cylindrical grain misoriented by 15°, 30° and 45° relative to the outer grain, Fig. 18. As the misorientation between the two grains increased, the differences in total dislocation densities from one grain to the other increased: 12%, 23% and 27% for the 15°, 30° and 45° cases, respectively.

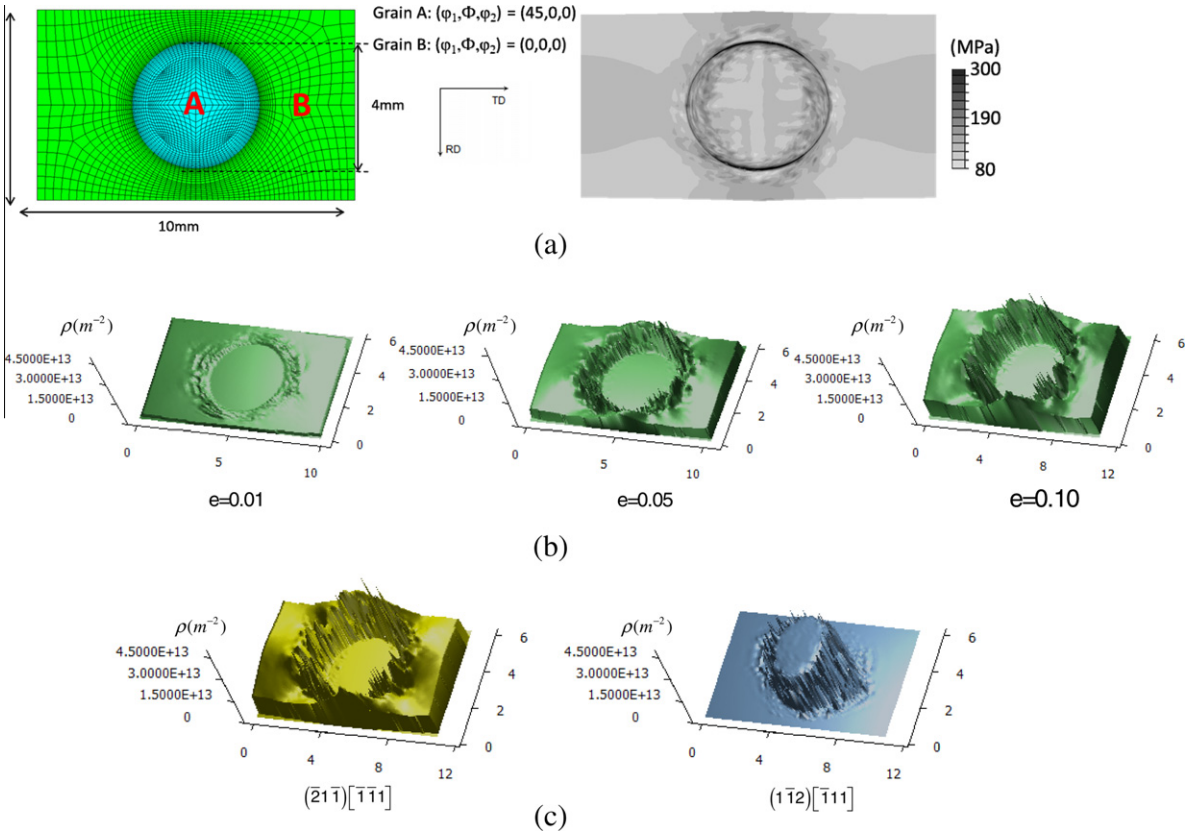


**Fig. 17.** Two-scale simulation of a virtual tensile specimen consisting of a cylindrical grain within a rectangular grain with the grains misoriented by 45° as shown: (a) schematic of mesh and specimen geometry, with Mises stress contours at 10% strain, (b) evolution of total dislocation densities at three strains – 1%, 5% and 10%, and (c) dislocation densities for two slip systems at a strain of 10%.

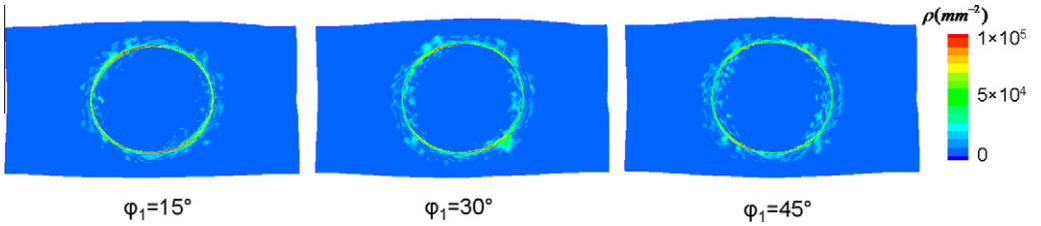


**Fig. 18.** Dislocation densities at 10% strain for the inner grain misoriented relative to the surrounding rectangular grain by 15°, 30° and 45°.

### 5.2. Bauschinger effect

In order to investigate the effect of the back stress on the reverse loading, simulations of a compression-tension test were conducted using the two-scale model. Parametric tests were performed using an imaginary square columnar polycrystal with 16 grains having four random crystal orientations (A–D) as shown in Fig. 19. Material constants for minimum alloy steel as used are listed in Table 6.

Fig. 20 shows simulated uniaxial compression and compression-tension tests with stress reversals at 1%, 3%, and 5% strains. Contrary to most conventional continuum models, e.g. PAN model, the two-scale model predicted lower yield stress at the reversal loading because of a developed back stress. The two-scale model does not require fitting parameters to obtain the back stress or its evolution; it is explicitly obtained from interaction forces among dislocations, Eq. (18).

### 5.3. Efficiency and mesh independence of the model

The two-scale model is computationally efficient. The CPU times required to simulate 64 grains with 8000 elements was 6.5 h, as compared to 13.5 h for the FE equilibration of dislocation content (see Section 2.3) for the same configuration.

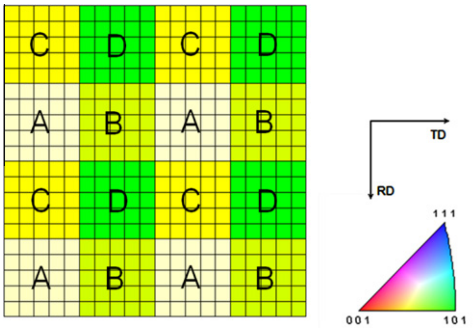


| Grain | $\varphi_1$ | $\Phi$ | $\varphi_2$ |
|---|---|---|---|
| A | 56.66 | 62.97 | 185.38 |
| B | 130.72 | 35.24 | 10.28 |
| C | 259.85 | 25.34 | 357.48 |
| D | 353.88 | 131.70 | 271.78 |

**Fig. 19.** Square columnar 16-grain polycrystal sample used to simulate compression-tension tests. Crystal orientations for each grain are shown in terms of Bunge's Euler angles (°).

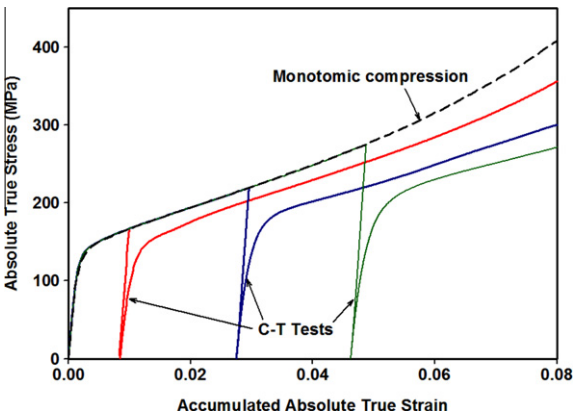


**Fig. 20.** Two-scale model simulated uniaxial compression and compression–tension tests of 16 grain square sample (Fig. 19) with 1%, 3% and 5% pre-strains. Material properties are for minimum alloy steel as presented in Tables 5 and 6.

**Table 10**
Comparison of simulation performance using four finite element meshes for a 4-grain specimen deformed to 1% strain.

| | 4500 Elements | 8000 Elements | 12,500 Elements | 18,000 Elements |
|---|---|---|---|---|
| Resolution (μm) | $33 \times 33 \times 20$ | $25 \times 25 \times 20$ | $20 \times 20 \times 20$ | $17 \times 17 \times 20$ |
| CPU time (h) | 0.7 | 1.3 | 2.1 | 2.8 |
| Eng. stress (MPa) | 147 | 145 | 143 | 142 |
| $\rho_{avg.}$ ($m^{-2}$) | $1.2 \times 10^{12}$ | $1.2 \times 10^{12}$ | $1.2 \times 10^{12}$ | $1.2 \times 10^{12}$ |
| $\rho_{max.}$ ($m^{-2}$) | $1.8 \times 10^{12}$ | $1.7 \times 10^{12}$ | $1.7 \times 10^{12}$ | $1.7 \times 10^{12}$ |
| Std. dev. of $\rho$[a] | $3.7 \times 10^{10}$ | $2.7 \times 10^{10}$ | $1.7 \times 10^{10}$ | – |

[a] The standard deviation of averaged dislocation density for 500 coinciding volumes (100 μm×100 μm×20 μm) for each mesh compared to the 18,000-element mesh was obtained using the following equation: $\text{Std.dev.} = \sqrt{\frac{\sum_{i=1}^{500}(\rho_i^{xele} - \rho_i^{1800ele})^2}{500}}$.

Computational time for the GSS alone was 6.2 h so the MSS procedure constituted only 5% of the total CPU time. Therefore, two-scale model is an efficient method, suitable for treating 100 or more grains even using a standard personal computer.

In order to test the mesh independence of the two-scale model, a 2D grain assembly having four grains (Fig. 13(a)) strained up to 1% was simulated using 4500, 8000, 12,500 and 18,000 elements ($30 \times 30 \times 5$, $40 \times 40 \times 5$, $50 \times 50 \times 5$, and $60 \times 60 \times 5$ elements). CPU times and engineering stresses for each case are listed in Table 10. The two-scale model showed small mesh dependence; engineering stresses showed 3% difference between 4500 and 18,000 elements, 147 MPa and 142 MPa, while average dislocation densities had negligible difference. In order to compare the dislocation densities corresponding to each mesh size in more detail, the sample was divided into 500 volumes (100 μm×100 μm×20 μm) and the standard deviation of the average dislocation density within each volume was calculated, with the results shown in Table 10. The standard deviation was less than 2% of the average dislocation density. The maximum dislocation densities among all the finite elements in the 4500 and 18,000 element models were within 5% of each other.

## 6. Conclusions

A novel two-scale model was developed linking single-crystal continuum constitutive equations at the grain and polycrystal scale to meso-scale evolution of dislocation densities on slip systems consistent with slip activity. Predictions were compared with several kinds of experiments. The following conclusions were reached:

(1) For the first time, a Hall–Petch slope was predicted within the experimental and simulation scatter, with no arbitrary length scales. The simulated Hall–Petch slopes for iron were $1.2 \pm 0.3$ and $1.5 \pm 0.3$ MN/m$^{3/2}$ for 2D and 3D grain assemblies, respectively while the corresponding measured slope was $0.9 \pm 0.1$ MN/m$^{3/2}$. Three parameters related to the strain hardening of a single crystal represent the only fit parameters. They were determined from a single tensile test, and their values do not affect the predicted Hall–Petch slope significantly.
(2) The model is practical and efficient. The CPU time to simulate 64 grains with 8000 finite elements deformed to a strain of 10% was 6.5 h, 5% greater than the corresponding FE-only simulation.
(3) The model accurately predicted the strain hardening of five multi-crystal tensile samples having 9–39 grains. The standard deviations of the predictions was 6 MPa, as compared with 17–19 MPa for equivalent standard FE models or Taylor texture-type models fit using the same procedures.
(4) The deviations of standard FE or Taylor models increase as the grain size varies from the fit one. The discrepancy presumably arises from neglecting the effect of grain boundaries on plastic deformation, inherent in these models. Such models predict no Hall–Petch effect.
(5) The model accurately predicted maximum lattice curvature for a Fe-3% Si specimen deformed to 8% strain. The maximum lattice curvature predicted by the two-scale model is $9.5 \times 10^{-3}$ rad/μm while the measured value is $9.2 \times 10^{-3}$ rad/μm, the difference being less than 5%.
(6) The model reproduces analytical and FE pile-up results without mesh dependence for sufficiently small elements.
(7) The only critical parameter affecting simulation results is the maximum grain boundary obstacle stress, $\tau^*$. The initial dislocation density has a smaller effect, and other parameters are insignificant.
(8) Spatial distributions of dislocation densities on each slip system in a polycrystal have been presented quantitatively. Significant accumulation of dislocations near grain boundaries occurs for some slip systems and grain boundaries.

## Acknowledgements

This work was made possible by NSF Grant 0936340, and the support of Alan Ardell in providing an EAGER award. The authors would like to thank John P. Hirth for helpful discussions and Craig S. Hartley for discussions as well as early support via AFOSR. Rob Comstock and Ron Hughes participated in early discussions and provided the Fe-3% Si and minimum alloy

steels used in this work, respectively. The authors also appreciate Josh Kacher for the sample preparations and OIM measurements.

## Appendix A:. Grain orientations for six minimum alloy steel samples

| Grain | $\varphi_1$ | $\Phi$ | $\varphi_2$ | Grain | $\varphi_1$ | $\Phi$ | $\varphi_2$ | Grain | $\varphi_1$ | $\Phi$ | $\varphi_2$ |
|---|---|---|---|---|---|---|---|---|---|---|---|
| *Sample 1* | | | | | | | | | | | |
| 1 | 62.6 | 20.0 | 276.3 | 4 | 354.6 | 17.9 | 332.9 | 7 | 305.0 | 42.6 | 55.7 |
| 2 | 161.2 | 44.3 | 236.0 | 5 | 90.1 | 35.1 | 233.9 | 8 | 160.4 | 48.5 | 209.7 |
| 3 | 34.0 | 20.9 | 302.5 | 6 | 112.3 | 45.1 | 253.5 | 9 | 286.2 | 27.7 | 91.8 |
| *Sample 2* | | | | | | | | | | | |
| 1 | 95.9 | 2.5 | 292.2 | 6 | 199.6 | 33 | 192 | 11 | 147 | 44.3 | 256.5 |
| 2 | 220.1 | 16.8 | 148.3 | 7 | 104.9 | 26.2 | 237.7 | 12 | 341.6 | 49.4 | 51.8 |
| 3 | 233.8 | 26.9 | 138.2 | 8 | 293.6 | 42.7 | 50.2 | 13 | 48.2 | 40.6 | 311.4 |
| 4 | 201.9 | 39.2 | 140.4 | 9 | 129.3 | 28.3 | 212.4 | | | | |
| 5 | 74.3 | 25.4 | 273.2 | 10 | 152.7 | 28.3 | 201.6 | | | | |
| *Sample 3* | | | | | | | | | | | |
| 1 | 189.7 | 50.5 | 180.7 | 7 | 241 | 15.8 | 87.8 | 13 | 197.5 | 23.5 | 151.1 |
| 2 | 103.8 | 43.9 | 211.6 | 8 | 23.6 | 19.7 | 306.3 | 14 | 191.6 | 575 | 192.2 |
| 3 | 24.3 | 4.2 | 327.2 | 9 | 172.8 | 33.6 | 214.1 | 15 | 207.8 | 13.5 | 131.4 |
| 4 | 283.0 | 13.7 | 43.1 | 10 | 15.9 | 18.7 | 2.6 | 16 | 220.0 | 22.1 | 121.8 |
| 5 | 253.5 | 40.3 | 140.7 | 11 | 273.9 | 20.6 | 84.5 | 17 | 266.3 | 20.3 | 124.1 |
| 6 | 246.1 | 36.7 | 104.9 | 12 | 43.5 | 30.5 | 357.2 | | | | |
| *Sample 4* | | | | | | | | | | | |
| 1 | 108.6 | 46.7 | 244.4 | 12 | 180.0 | 44.6 | 225.1 | 23 | 285.9 | 43.0 | 33.0 |
| 2 | 1.2 | 22.3 | 28.2 | 13 | 178.2 | 44.5 | 138.7 | 24 | 163.4 | 50.6 | 226.9 |
| 3 | 324.5 | 19.7 | 352.1 | 14 | 194.0 | 45.9 | 130.5 | 25 | 94.4 | 37.0 | 267.1 |
| 4 | 284.6 | 43.8 | 103.8 | 15 | 2.7 | 32.9 | 36.9 | 26 | 155.0 | 37.8 | 195.7 |
| 5 | 121.5 | 49.6 | 256.9 | 16 | 168.2 | 47.0 | 144.3 | 27 | 89.3 | 36.6 | 263.6 |
| 6 | 116.0 | 44.8 | 261.1 | 17 | 306.0 | 42.3 | 12.6 | 28 | 284.7 | 39.6 | 39.7 |
| 7 | 234.4 | 37.0 | 151.4 | 18 | 181.3 | 37.3 | 223.0 | 29 | 22.3 | 42.0 | 309.9 |
| 8 | 155.0 | 20.7 | 251.2 | 19 | 295.4 | 44.1 | 26.2 | 30 | 196.0 | 36.9 | 134.0 |
| 9 | 164.7 | 28.9 | 152.4 | 20 | 57.0 | 52.1 | 326.1 | 31 | 17.1 | 36.0 | 313.5 |
| 10 | 157.5 | 32.7 | 157.9 | 21 | 23.0 | 18.5 | 9.3 | 32 | 310.2 | 49.1 | 66.9 |
| 11 | 170.0 | 36.6 | 146.4 | 22 | 358.4 | 14.5 | 32.1 | | | | |
| *Sample 5* | | | | | | | | | | | |
| 1 | 55.8 | 52.5 | 331.0 | 13 | 40.2 | 11.9 | 322.0 | 25 | 86.8 | 38.6 | 271.9 |
| 2 | 59.8 | 57.0 | 321.0 | 14 | 169.6 | 30.6 | 170.3 | 26 | 259.1 | 37.4 | 102.3 |
| 3 | 218.2 | 42.2 | 181.3 | 15 | 71.0 | 18.3 | 296.4 | 27 | 283.1 | 34.6 | 72.3 |
| 4 | 58.8 | 60.9 | 298.1 | 16 | 81.5 | 28.7 | 285.3 | 28 | 128.7 | 23.2 | 227.9 |
| 5 | 38.0 | 41.9 | 357.5 | 17 | 138.7 | 16.5 | 215.0 | 29 | 350.1 | 40.3 | 6.6 |
| 6 | 226.1 | 33.8 | 175.4 | 18 | 93.8 | 14.6 | 271.8 | 30 | 198.7 | 2.9 | 194.4 |
| 7 | 167.3 | 21.5 | 202.4 | 19 | 74.9 | 46.1 | 281.0 | 31 | 355.7 | 21.1 | 44.2 |
| 8 | 200.4 | 24.5 | 161.5 | 20 | 254.8 | 36.4 | 102.5 | 32 | 330.7 | 49.6 | 28.9 |
| 9 | 180.6 | 33.2 | 184.9 | 21 | 84.3 | 7.1 | 318.3 | 33 | 329.9 | 12.8 | 66.2 |
| 10 | 71.5 | 37.9 | 293.1 | 22 | 248.3 | 32.2 | 110.5 | 34 | 202.8 | 27.1 | 140.7 |
| 11 | 239.5 | 11.2 | 160.6 | 23 | 258.2 | 36.1 | 96.8 | | | | |
| 12 | 77.6 | 43.2 | 297.2 | 24 | 272.1 | 26.8 | 80.7 | | | | |
| *Sample 6* | | | | | | | | | | | |
| 1 | 59.7 | 30.7 | 301.0 | 14 | 306.5 | 51.1 | 30.9 | 27 | 162.6 | 38.8 | 189.0 |
| 2 | 353.0 | 13.3 | 26.9 | 15 | 294.0 | 19.6 | 97.7 | 28 | 358.6 | 10.2 | 14.9 |
| 3 | 24.2 | 15.0 | 357.3 | 16 | 54.4 | 54.1 | 326.9 | 29 | 163.1 | 1.6 | 212.4 |
| 4 | 326.9 | 37.9 | 40.8 | 17 | 261.7 | 18.0 | 111.7 | 30 | 215.7 | 36.1 | 152.9 |
| 5 | 44.9 | 52.9 | 299.0 | 18 | 43.5 | 45.7 | 315.8 | 31 | 297.3 | 20.2 | 21.6 |

(*continued on next page*)

**Appendix A** (*continued*)

| Grain | $\varphi_1$ | $\Phi$ | $\varphi_2$ | Grain | $\varphi_1$ | $\Phi$ | $\varphi_2$ | Grain | $\varphi_1$ | $\Phi$ | $\varphi_2$ |
|---|---|---|---|---|---|---|---|---|---|---|---|
| 6 | 318.7 | 9.0 | 61.2 | 19 | 237.4 | 14.5 | 137.5 | 32 | 226.5 | 13.8 | 173.1 |
| 7 | 293.8 | 29.0 | 106.5 | 20 | 4.6 | 43.0 | 343.4 | 33 | 225.3 | 16.2 | 172.9 |
| 8 | 218.1 | 23.4 | 129.7 | 21 | 87.7 | 34.5 | 310.3 | 34 | 74.0 | 38.5 | 285.0 |
| 9 | 189.1 | 37.8 | 161.9 | 22 | 207.9 | 22.8 | 167.8 | 35 | 239.5 | 39.3 | 75.9 |
| 10 | 281.5 | 31.0 | 73.6 | 23 | 48.1 | 20.4 | 349.2 | 36 | 336.3 | 43.1 | 6.6 |
| 11 | 21.1 | 31.1 | 22.6 | 24 | 225.1 | 46.9 | 119.3 | 37 | 260.7 | 20.9 | 124.6 |
| 12 | 24.1 | 36.5 | 346.6 | 25 | 133.2 | 8.0 | 246.6 | 38 | 134.6 | 15.0 | 204.7 |
| 13 | 109.8 | 44.7 | 237.2 | 26 | 291.9 | 41.3 | 71.7 | 39 | 102.4 | 36.8 | 287.9 |

## References


Abson, D.J., Jonas, J.J., 1970. Hall–Petch relation and high-temperature subgrains. Metal. Sci. J. 4, 24–28.
Abu Al-Rub, R.K., Voyiadijus, G.Z., 2006. A physically based gradient plasticity theory. Int. J. Plast. 22, 654–684.
Adams, B.L., Field, D.P., 1992. Measurement and representation of grain boundary texture. Metall. Trans. 23A, 2501–2513.
Adams, M.A., Roberts, A.C., Smallman, R.E., 1960. Yield and fracture in polycrystalline niobium. Acta Met. 8, 328.
Allen, B., Moore, A., 1963. The Metallurgy of Beryllium. Chapman and Hall, London.
Anand, L., Gurland, J., 1976. Effect of internal boundaries on the yield strengths of spheroidized steels. Met. Trans. A 7, 191.
Anderson, P.M., Shen, Y., 2006. Transmission of a screw dislocation across a coherent, slipping interface. Acta Mater. 54, 3941–3951.
Armstrong, R.W., Codd, I., Douthwaite, R.M., Petch, N.J., 1962. The plastic deformation of polycrystalline aggregates. Philos. Mag. 7, 45.
Arsenlis, A., Parks, D.M., Becker, R., Bulatov, V.V., 2004. On the evolution of crystallographic dislocation density in non-homogeneously deforming crystals. J. Mech. Phys. Solids 52, 1213.
Asaro, R.J., 1979. Geometrical effects in the inhomogeneous deformation of ductile single crystals. Acta Met. 27, 445.
Asaro, R.J., 1983. Micromechanics of crystals and polycrystals. Adv. Appl. Mech. 23, 1–115.
Asaro, R.J., Needleman, A., 1985. Texture development and strain hardening in rate dependent polycrystals. Acta Metall. 33, 923–953.
Ashby, M.F., 1970. Mechanical effects of a dispersion of a second phase. Phil. Mag. 21, 399.
Balint, D.S., Deshpande, V.S., Needleman, A., Van der Giessen, E., 2005. A discrete dislocation plasticity analysis of grain size strengthening. Mater. Sci. Eng. A, 186–190.
Balint, D.S., Deshpande, V.S., Needleman, A., Van der Giessen, E., 2008. Discrete dislocation plasticity analysis of the grain size dependence of the flow strength of polycrystals. Int. J. Plast. 24, 2149–2172.
Beaudoin, A.J., Dawson, P.R., Mathur, K.K., Kocks, U.F., Korzekwa, D.A., 1994. Application of polycrystal plasticity to sheet forming. Comput. Methods Appl. Mech. Eng. 117, 49–70.
Becker, R., Panchanadeeswaran, S., 1995. Effects of grain interactions on deformation and local texture in polycrystals. Acta Metall. Mater. 43 (7), 2701–2719.
Biner, S.B., Morris, J.R., 2003. The effects of grain size and dislocation source density on the strengthening behaviour of polycrystals, a two dimensional discrete dislocation simulation. Phil. Mag. 83, 3677–3690.
Bronkhorst, C.A., Kalidinidi, S.R., Anand, L., 1992. Polycrystalline plasticity and the evolution of crystallographic texture in FCC metals. Philos. Trans. Roy. Soc. London A 341 (443).
Canova, G.R., Kocks, U.F., Tome, C.N., Jonas, J.J., 1985. The yield surface of textured polycrystals. J. Mech. Phys. Solids 33, 371–397.
Carreker, R.P., 1957. Tensile deformation of silver as a function of temperature, strain rate, and grain size. Trans. AIME 209, 113.
Carreker, R.P., Hibbard, W.R., 1957. Temperature, strain rate, and grain size. Trans. AIME 209, 1157.
Chang, P.H., Preban, A.G., 1985. The effect of ferrite grain size and martensite volume fraction on the tensile properties of dual phase steel. Acta Metall. 33 (5), 897–903.
Choi, S.-H., Kim, D.H., Park, S.S., You, B.S., 2010. Simulation of stress concentration in Mg alloys using the crystal plasticity finite element method. Acta Mater. 58, 320–329.
Christian, J.W., Vitek, V., 1970. Dislocations and stacking faults. Rep. Prog. Phys. 33, 307.
Conrad, H., 1961. Electron Microscopy and Strength of Crystals. Interscience, New York.
Conrad, H., 1970. Ultrafine-Grain Metals. Syracuse University Press, Syracuse, New York.
Cottrell, A.H., 1953. Dislocations and plastic flow in crystals. Oxford University Press, London.
Dawson, P.R., Mika, D.P., Barton, N.R., 2002. Finite element modeling of lattice misorientations in aluminum polycrystals. Scripta Mater. 47 (10), 713–717.
Dawson, P.R., MacEwen, S.R., Wu, P.D., 2003. Advances in sheet metal forming analyses, dealing with mechanical anisotropy from crystallographic texture. Int. Mater. Rev. 48 (2), 86–122.
de Koning, M., Kurtz, R.J., Bulatov, V.V., Henager, C.H., Hoagland, R.G., Cai, W., Nomura, M., 2003. Modeling of dislocation-grain boundary interactions in FCC metals. J. Nucl. Mater. 323, 281–289.
De Messemaeker, J.V.B., Van Humbeek, J., 2004. On the strength of boundaries in submicron IF steel. Mater. Lett. 58, 3782–3786.
Delannay, L., Melchior, M.A., Signorelli, J.W., Remacle, J.-F., Kuwabara, T., 2009. Influence of grain shape on the planar anisotropy of rolled steel sheets – evaluation of three models. Comput. Mater. Sci. 45 (3), 739–743.
Dieter, G.E., 1976. Mechanical Metallurgy, second ed. McGraw Hill.
Duesbery, M.S., Richardson, G.Y., 1991. The dislocation core in crystalline materials. CRC Crit. Rev. Solid State Mater. Sci. 17, 1.
El-Dasher, B.S., Adams, B.L., Rollett, A.D., 2003. Viewpoint, experimental recovery of geometrically necessary dislocation density in polycrystals. Scripta Mater. 48, 141.
Esheby, J.D., Frank, F.C., Nabarro, F.R.N., 1951. The equilibrium of linear arrays of dislocations. Phil. Mag. 42, 351.
Evers, L.P., Parks, D.M., Brekelmans, W.A.M., Geers, M.G.D., 2002. Crystal plasticity model with enhanced hardening by geometrically necessary dislocation accumulation. J. Mech. Phys. Solids 50 (11), 2403–2424.
Evers, L.P., Brekelmans, W.A.M., Geers, M.G.D., 2004. Non-local crystal plasticity model with intrinsic SSD and GND effects. J. Mech. Phys. Solids 52, 2379–2401.
Feaugas, X., Haddou, H., 1999. On the origin of the tensile flow stress in the stainless steel AISI 316L at 300 K, Back stress and effective stress. Acta Mater. 47, 3617.
Feaugas, X., Haddou, H., 2003. Grain-size effects on tensile behavior of nickel and AISI 316L stainless steel. Met. Trans. A 34, 2329.

Feltham, P., Meakin, J.D., 1957. On the mechanism of work hardening in face-centred cubic metals, with special references to polycrystalline copper. Philos. Mag. 2, 105.
Fleck, N.A., Hutchinson, J.W., 1997. Strain gradient plasticity. Adv. Appl. Mech. 33, 295.
Fleck, N.A., Muller, G.M., Ashby, M.F., Hutchinson, J.W., 1994. Strain gradient plasticity, theory and experiment. Acta Metall. Mater. 42, 475.
Gao, H., Huang, Y., Nix, W.D., Hutchinson, J.W., 1999. Mechanism-based strain gradient plasticity I: theory. J. Mech. Phys. Solids 47, 1239–1263.
Grabski, M.W., Wyrzylowski, J.W., 1980. The effect of the spreading of grain boundary dislocations on the tensile behavior of a fine-grained austenitic steel at high temperatures. Mater. Sci. Eng. 44 (2), 229–237.
Groma, I., 1997. Link between the microscopic and mesoscopic length-scale description of the collective behavior of dislocations. Phys. Rev. B 56 (10), 5807–5813.
Gubicza, J., Chinh, N.Q., Lábár, J.L., Dobatkin, S., Hegedüs, Z., Langdon, T.G., 2009. Correlation between microstructure and mechanical properties of severely deformed metals. J. Alloys Compd. 483, 271–274.
Gurtin, M.E., 2000. On the plasticity of single crystals, free energy, microforces, plastic strain gradients. J. Mech. Phys. Solids (48), 989.
Gurtin, M.E., 2002. A gradient theory of single-crystal viscoplasticity that accounts for geometrically necessary dislocations. J. Mech. Phys. Solids (50), 5.
Hall, E.O., 1951. The deformation and ageing of mild steel. Proc. Roy. Soc. London B64, 747.
Hartley, C.S., 2003. A method for linking thermally activated dislocation mechanisms of yielding with continuum plasticity theory. Phil. Mag. 83, 3783.
Hauser, F.E., Landon, P.R., Dorn, J.E., 1956. Fracture of magnesium alloys at low temperature. Trans. AIME 206, 589.
Hibbit, K.S.I., 2005. ABAQUS/Standard User's Manual.
Hill, R., Rice, J.R., 1972. Constitutive analysis of elastic plastic crystals at arbitrary strain. J. Mech. Phys. Solids 20 (401).
Hirth, J.P., 1972. Influence of grain boundaries on mechanical properties. Met. Trans. 3, 3047.
Hirth, J.P., Lothe, J., 1969. Theory of Dislocations. McGraw-Hill, New York.
Hoagland, R.G., Kurtz, R.J., 2002. The relation between grain-boundary structure and sliding resistance. Philos. Mag. 82 (6), 1073–1092.
Hoagland, R.G., Mitchell, T.E., Hirth, J.P., Kung, H., 2002. On the strengthening effects of interfaces in multilayer fcc metallic composites. Philos. Mag. 82 (4), 643–664.
Hoagland, R.G., Kurtz, R.J., Henager Jr., C.H., 2004. Slip resistance of interfaces and the strength of metallic multilayer composites. Scripta Mater. 50, 775–779.
Huang, Y., Gao, H., Nix, W.D., Hutchinson, J.W., 2000. Mechanism-based strain gradient plasticity II. Anal. J. Mech. Phys. Solids 48, 99–128.
Hull, D., 1975. Effect of grain size and temperature on slip twinning and fracture in 3% silicon iron. Acta Met. 9, 191–204.
Hutchinson, J.W., 1976. Bounds and self-consistent estimates for creep of polycrystalline materials. Proc. Roy. Soc. London A348, 1465–1469.
Johnson, A.A., 1959. The effect of grain size on the tensile properties of high-purity molybdenum at room temperature. Philos. Mag. 4, 194.
Kalidindi, S.R., Bronkshorst, C.A., Anand, L.J., 1992. Crystallographic texture evolution in bulk deformation processing of FCC metals. J. Mech. Phys. Solids 40 (537).
Kassner, M.E., 1990. A case for Taylor hardening during primary and steady-state creep in aluminium and type 304 stainless steel. J. Mater. Sci. 25, 1997–2003.
Keeler, J.H., 1955. The tensile characteristics of unalloyed zirconium at low and moderate temperatures. Trans. AIME 47, 157.
Keh, A.S., 1961. Electron Microscopy and Strength of Crystals. Interscience, New York.
Kocks, U.F., 1959. Comments on yield strength of metals as a function of grain size. Acta Metall. 7, 131.
Kocks, U.F., 1970. The relation between polycrystal deformation and single crystal deformation. Metall. Trans. 1, 1121–1143.
Kocks, U.F., 1976. Laws for work-hardening and low-temperature creep. J. Eng. Mater. Tech., ASMEH 98, 76.
Koo, R.C., 1962. Grain-size effects on the deformation of tantalum at low temperatures. J. Less Common Met. 4 (2), 138–144.
Kröner, E., 1961. Zur Plastichen Verformung des Vielkristalls. Acta Metall. 9 (155).
Lee, E.H., 1969. Elastic–plastic deformation at finite strains. J. Appl. Mech. 36 (1).
Lee, M.G., Lim, H., Adams, B.L., Hirth, J.P., Wagoner, R.H., 2010. A dislocation density-based single crystal constitutive equation. Int. J. Plast. 26, 925–938.
Lefebvre, S., Devincre, B., Hoc, T., 2005. Simulation of the Hall–Petch effect in ultra-fine grained copper. Mater. Sci. Eng. A, 150–153.
Lefebvre, S., Devincre, B., Hoc, T., 2007. Yield stress strengthening in ultrafine-grained metals, A two dimensional simulation of dislocation dynamics. J. Mech. Phys. Solids 55, 788–802.
Leibfried, G., 1951. Verteilung von Versetzungen im statischen Gleichgewicht. Z. Phys. 130, 214.
Li, J.C.M., 1963. A dislocation mechanism of transient creep. Acta Metall. 11, 1269.
Li, J.C.M., Chou, Y.T., 1970. The role of dislocations in the flow stress-grain size relationship. Met. Trans. 1, 1145.
Li, Z., Hou, C., Huang, M., Ouyang, C., 2009. Strengthening mechanism in micro-polycrystals with penetrable grain boundaries by discrete dislocation dynamics simulation and Hall–Petch effect. Comput. Mater. Sci. 46, 1124–1134.
Lim, H., Lee, M.G., Kim, J.H., Hirth, J. P., Adams, B.L., Wagoner, R.H., 2010. Prediction of polycrystal deformation with a novel multi-scale approach. In: 1st Conf. Adv. Interaction and Multiscale Mech., AIMM'10.
Lindley, F.C., Smallman, R.E., 1963. The determination of the yield stress parameters $K_y$ and $\sigma_i$, by grain-size and extrapolation methods. Acta Metall. 11, 626.
Livingston, J.D., Chalmers, B., 1957. Multiple slip in bi-crystal deformation. Acta Metall. 5, 322.
Ma, A., Roters, F., Raabe, D., 2006. Studying the effect of grain boundaries in dislocation density based crystal-plasticity finite element simulations. Int. J. Solid Struct. 43, 7287–7303.
Marcinkowski, M.J., Lipsitt, H.A., 1962. The plastic deformation of chromium at low tempeartures. Acta. Met. 10, 95.
Meieran, E.S., Thomas, D.A., 1965. Structure of drawn and annealed tungsten wire. Trans. AIME 233, 937.
Meyers, M.A., Ashworth, E., 1982. A model for the effect of grain size on the yield stress of metals. Phil. Mag. A 46 (5), 737–759.
Meyers, M.A., Chawla, K.K., 1998. Mechanical Behavior of Materials. Prentice-Hall, Upper Saddle.
Molinari, A., Canova, G.R., Ahzi, S., 1987. A self consistent approach of the large deformation polycrystal viscoplasticity. Acta Metall. 35, 2983–2994.
Nembach, E., 1990. The dependence of the Hall–Petch slope on the ('-precipitate dispersion of polycrystals of a nickel-base superalloy. Scr. Metall. Mater. 24 (4), 787–792.
Nix, W.D., Gao, H., 1998. Indentation size effects in crytalline materials, a law for strain gradient plasticity. J. Mech. Phys. Solids 46, 411–425.
Nye, J.F., 1953. Some gemetrical relations in dislocated crystals. Acta metall. 1, 153.
Ohashi, T., Kawamukai, M., Zbib, H., 2007. A multiscale approach for modeling scale-dependent yield stress in polycrystalline metals. International Journal of Plasticity 23, 897–914.
Olivares, F. H., Sevillano. J. Gil., 1987. A quantitative assessment of forest hardening in FCC materials. Acta. Met. 35, 631-641.
Orlová, A., 2004. Relation between the internal stress measured in creep and the stress generated by the dislocation structure in the fcc metals. Philos. Mag. 11 (84), 3419–3426.
Orowan, E., 1940. Problems of plastic gliding. Proc. Phys. Soc. 52, 8–22.
Parks, D.M., Ahzi, S., 1990. Polycrystalline plastic deformation and texture evolution for crystals lacking five independent slip systems. J. Appl. Phys. Solids 38, 701–724.
Peirce, D., Asaro, R.J., Needleman, A., 1982. An analysis of nonuniform and localized deformation in ductile single crystals. Acta Metall 30, 1087.
Peirce, D., Asaro, R.J., Needleman, A., 1983. Materials rate dependence and localized deformation in crystalline solids. Acta metall. 31, 1951–1976.
Petch, N.J., 1953. The cleavage strength of polycrystals. J. Iron Steel Inst. 174, 25–28.
Raabe, D., Klose, P., Engl, B., Imlau, K.P., Friedel, F., Roters, F., 2002. Concepts for integrating plastic anisotropy into metal forming simulation. Adv. Eng. Mater. 4 (4), 18–169.
Rice, J.R., 1971. Inelastic constitutive relations for solids, an internal-variable theory and its application to metal plasticity. J. Mech. Phys. Solids 19 (433).

Russell, B., 1965. The influence of grain size on the flow stress of a copper-3.2 at.% tin solid solution. Acta Met. 13, 11.
Saada, G., 2005. From the single crystal to the nanocrystal. Phil. Mag. 85 (25–26), 3003–3018.
Sachs, G., 1928. Zur Ableitung Einer Fliessbedingung. Z. Ver. Dtsch. Ing. 12, 134–136.
Sarma, G.B., Dawson, P.R., 1996. Effects of interactions among crystals on the inhomogeneous deformations of polycrystals. Acta Mater. 44 (5), 1937–1953.
Sarma, G.B., Radhakrishnan, B., Dawson, P.R., 2002. Mesoscale modeling of microstructure and texture evolution during deformation processing of metals. Adv. Eng. Mater. 4 (7), 509–514.
Schafler, E., Simon, K., Bernstorff, S., Hanák, P., Tichy, G., Ungár, T., Zehetbauer, M.J., 2005. A second-order phase-transformation of the dislocation structure during plastic deformation determined by in situ synchrotron X-ray diffraction. Acta. Mater. 53, 315–322.
Schoeck, G., Frydman, R., 1972. The contribution of the dislocation forest to the flow stress. Phys. Stat. Sol. B 53, 661.
Shen, Z., Wagoner, R.H., Clark, W.A.T., 1986. Dislocation pile-up and grain boundary interactions in 304 stainless steel. Scripta Metall. 20, 921.
Shen, Z., Wagoner, R.H., Clark, W.A.T., 1988. Dislocation and grain boundary interactions in metals. Acta Metal. 36 (12), 3231–3242.
Stolken, J.S., Evans, A.G., 1998. A microbend test method for measuring the plasticity length-scale. Acta Mater. 46, 5109–5115.
Sun, S., Adams, B.L., King, W.E., 2000. Observation of lattice curvature near the interface of a deformed aluminum bicrystals. Phil. Mag. A (80), 9.
Taylor, G.I., 1934. The mechanism of plastic deformation of crystals. Proc. Roy. Soc. A165, 362.
Tsuji, N., Ito, Y., Ueji, R., Minamino, Y., Koizumi, Y., Saito, Y., 2001. Mechanical properties of ultrafine grained ferritic steels produced by accumulative roll-bonding (ARB) process. In: ISUGS 2001, International Symposium on Ultrafine Grained Steels, Fukuoka; Japan.
Vitek, V., 1992. Structure of dislocation cores in metallic materials and its impact on their plastic behaviour. Prog. Mater. Sci. 36, 1.
Vitek, V., Mrovec, M., Bassani, J.L., 2004. Influence of non-glide stresses on plastic flow, from atomistic to continuum modeling. Mater. Sci. Eng. A 365, 31–37.
Wagoner, R.H., Yao, Z.C., Wu, Q., 1998. Finite element analysis of plastic yielding in Fe-3% Si bicrystals, boundaries and interfaces in materials. In: The David A. Smith Symposium, TMS, Warrendale, PA.
Widersich, H., 1964. Hardening mechanisms and the theory of deformation. J. Met. 16, 423.
Yefimov, S.G.I., van der Giessen, E., 2004. A comparison of a statistical-mechanics based plasticity model with discrete dislocation plasticity calculations. J. Mech. Phys. Solids 52, 279–300.
Zerilli, F.J., Armstrong, R.W., 1990. Description of tantalum deformation by dislocation mechanics based constitutive equations. J. Appl. Phys. 68 (4), 1580–1591.
Zhao, M.C., Hanamura, T., Qiu, H., Nagai, K., Yang, K., 2006. Grain growth and Hall–Petch relation in dual-sized ferrite/cementite steel with nano-sized cementite particles in a heterogeneous and dense distribution. Scripta Mater. 54, 1193–1197.
Zoqui, E.J., Robert, M.H., 1998. Structural modifications in rheocast Al–Cu alloys by heat treatment and implications on mechanical properties. J. Mater. Proc. Tech. (Netherlands) 78 (1–3), 198–203.